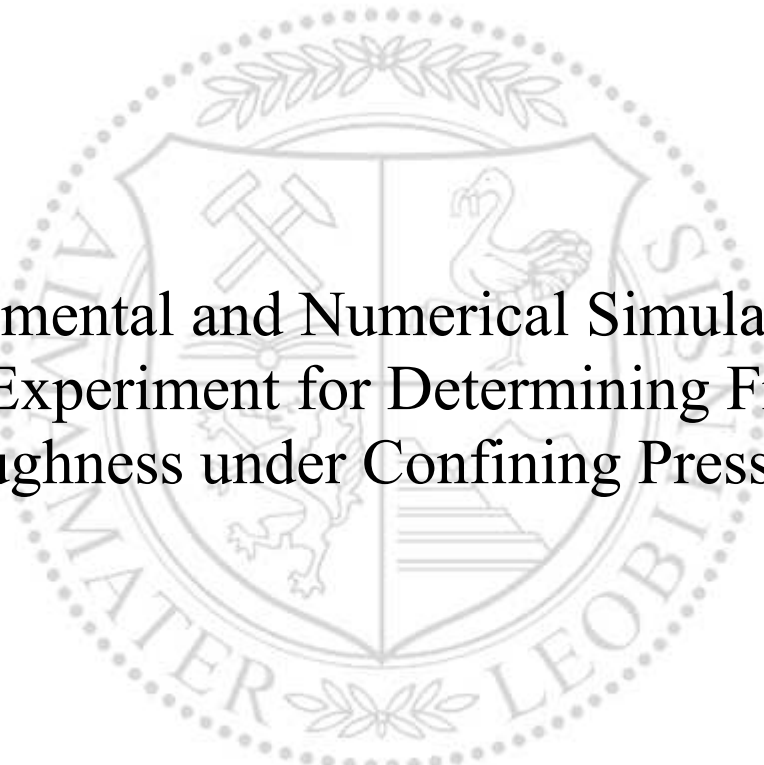Chair of Subsurface Engineering

Master's Thesis

Experimental and Numerical Simulation of Burst Experiment for Determining Fracture Toughness under Confining Pressure

Onur Inal

May 2024

EIDESSTATTLICHE ERKLÄRUNG

Ich erkläre an Eides statt, dass ich diese Arbeit selbstständig verfasst, andere als die angegebenen Quellen und Hilfsmittel nicht benutzt, den Einsatz von generativen Methoden und Modellen der künstlichen Intelligenz vollständig und wahrheitsgetreu ausgewiesen habe, und mich auch sonst keiner unerlaubten Hilfsmittel bedient habe.

Ich erkläre, dass ich den Satzungsteil „Gute wissenschaftliche Praxis" der Montanuniversität Leoben gelesen, verstanden und befolgt habe.

Weiters erkläre ich, dass die elektronische und gedruckte Version der eingereichten wissenschaftlichen Abschlussarbeit formal und inhaltlich identisch sind.

Datum 05.05.2024

_____
Unterschrift Verfasser/in
Onur Inal

Foreword

Life is a journey full of unexpected twists and turns. I want to extend my sincere gratitude to all the people who have shed light on my journey and steered me towards the right path.

First and foremost, I would like to thank my family for raising me and always supporting my goals throughout my life. They have always believed in my abilities as an engineer and never doubted my determination to study and work in this field.

Here, I would like to express my deepest admiration for my supervisor, Villeneuve, Marlene, Assoc. Prof., Phd, who provided me the opportunity to work on this challenging research project. This master thesis would not have been possible without her trust and support for any decisions I made. Thank you for guiding me and inspiring me during my studies and this research project.

I would also like to thank Yoshioka, Keita, Univ.-Prof. PhD, who encouraged me to go to the University of Pittsburgh to conduct the laboratory experiments for my master thesis. Our numerous discussions were greatly helpful to me. The training I obtained from him benefited me so much in my research. He is the kind of advisor who is constantly ready to offer genuine assistance.

Thanks also to Bunger, Andrew, Assoc. Prof., Phd, who was my first contact at the University of Pittsburgh Swanson School of Engineering and my supervisor during my stay there. I also appreciate the support of his research group and the staff of the civil and environmental engineering faculty. Hager Charles (Scooter), Lu Guanyi and Hartz Olivia have helped me to solve numerous challenges encountered during the lab experiments.

Finally, I am grateful to my friends at the University of Leoben, who made my studying and living experience in Austria great. They have all supported me unconditionally throughout challenging times.

Abstract

The burst experiment is a common method that is mostly used in the petroleum industry to estimate the fracture toughness (K_{IC}) of rocks under confinement in the laboratory. Unlike other methods, it tests rock samples subjected to confining stress, which represents the actual subsurface condition of a stressed wellbore with bi-wing fractures, and therefore it is considered advantageous to other methods. Fracture propagation in this burst experiment is only indicated by a sudden burst of the jacketed sample, where the burst pressure is measured. The fracture toughness of the sample can then be calculated after taking this recorded pressure as the critical pressure required to propagate the axially pre-notched wing fractures. However, the fracture growth may exist before the sample bursts, which might be a possible weakness of this technique. The cause is the existence of stable crack growth before the unstable "burst". Due to the challenges in the detection of this stable crack growth, there is significant uncertainty in the crack length used in the analysis of the results.

The purpose of this thesis is to estimate fracture toughness accurately by comparing the stable and unstable behavior types from numerical modeling predictions with the results of a series of modified burst experiments using acoustic emission (AE) detection for certain configurations. The results indicate that stable growth will occur before sample rupture for certain sample geometry and loading combinations. The difference between stable and unstable growth cases is detected from acoustic emission monitoring records. Moreover, modifications are proposed for more accurate fracture toughness calculations after investigating the behavior of the estimated fracture toughness results. More consistent estimations of fracture toughness are obtained from experiments with unstable configurations. The results of experiments with unstable behavior indicate a positive correlation between confining pressure and fracture toughness estimations, which complies with many observations reported in the literature. Lastly, fixed confinement experiments are performed for a legitimate calculation of K_{IC} with a range of geometry and loading conditions based on the global stability criterion. The effect of fixed confining pressure on the fracture toughness estimations has been shown, offering guidance for improved design of this frequently used test method.

Kurzfassung

Der Berstversuch ist eine gängige Methode, welche vor allem in der Erdölindustrie zur Abschätzung der Bruchzähigkeit (K_{IC}) von Gestein unter Einspannung im Labor verwendet wird. Im Gegensatz zu anderen Methoden werden hier Gesteinsproben unter Spannung geprüft, was den tatsächlichen Untergrundbedingungen eines belasteten Bohrlochs mit zweiflügeligen Brüchen entspricht und daher als vorteilhaft gegenüber anderen Methoden angesehen wird. Die Bruchausbreitung wird bei diesem Berstversuch nur durch ein plötzliches Bersten der eingespannten Probe angezeigt, wobei der Berstdruck gemessen wird. Die Bruchzähigkeit der Probe kann dann berechnet werden, indem dieser aufgezeichnete Druck als kritischer Druck für die Ausbreitung der axial vorgekerbten Flügelbrüche verwendet wird. Das Bruchwachstum kann jedoch bereits vor dem Bersten der Probe einsetzen, was eine mögliche Schwäche dieser Technik darstellt. Die Ursache ist das Vorhandensein eines stabilen Risswachstums vor dem instabilen „Bersten". Aufgrund der Schwierigkeiten bei der Erkennung dieses stabilen Risswachstums besteht eine erhebliche Unsicherheit in Bezug auf die Risslänge, die bei der Analyse der Ergebnisse verwendet wird.

Ziel dieser Arbeit ist es, die Bruchzähigkeit abzuschätzen, indem die stabilen und instabilen Verhaltenstypen aus numerischen Modellierungen mit den Ergebnissen von modifizierten Berstexperimenten unter Verwendung der akustischen Emissionsmessung (AE) verglichen wurden. Die Ergebnisse zeigen, dass bei bestimmten Probengeometrien und Belastungskombinationen ein stabiles Verhalten vor dem Bruch der Probe auftritt. Der Unterschied zwischen stabilem und instabilem Verhalten wird anhand der Aufzeichnungen der Schallemissionsüberwachung festgestellt. Darüber hinaus werden Vorschläge für genauere Bruchzähigkeitsberechnungen anhand der Ergebnisse der Bruchzähigkeitsversuche dargestellt. Aus Experimenten mit instabilen Konfigurationen werden konsistentere Schätzungen der Bruchzähigkeit gewonnen. Die Ergebnisse von Experimenten mit instabilem Verhalten deuten auf eine positive Korrelation zwischen dem Umschließungsdruck und den Schätzungen der Bruchzähigkeit hin, was mit vielen in der Literatur gemachten Beobachtungen übereinstimmt. Schließlich werden Experimente mit konstantem Umschließungsdruck für eine legitime Berechnung des K_{IC} mit einer Reihe von Geometrien und Belastungsbedingungen auf der Grundlage des globalen Stabilitätskriteriums durchgeführt. Es wurde gezeigt, wie sich ein konstanter Umschließungsdruck auf die Schätzungen der Bruchzähigkeit auswirkt, was Anhaltspunkte für eine verbesserte Auslegung dieser häufig verwendeten Prüfmethode bietet.

Table of Contents

List of Tables

List of Figures

Abbreviations

K_I^{B*} .... Stress intensity factor

a .... Inner radius

AE... Acoustic emission

b .... Outer radius

CDISK ....Chevron notched disk specimen

G_c .... Critical energy release rate

HDT .... Hit definition time

HLT .... Hit lockout time

K_I .... Stress intensity factor

K_{IC} ....Fracture toughness

ℓ .... Normalized crack length

LEFM .... Linear elastic fracture mechanics

OGS ....OpenGeoSys

p^* .... Ratio of the outer pressure to inner pressure

PDT.. Peak definition time

P_i .... Inner pressure

P_{ic} .... Critical inner pressure

P_o ....Outer pressure

SIF.. Stress intensity factor

THMC .... Thermo hydro mechanical chemical

w .... Ratio of the outer radius to inner radius

l_0 .... Initial fracture length

1 Introduction

Rock fracturing has always been one of the most important topics in rock mechanics, and fracture networks play a key role, particularly in geothermal energy production, storing carbon dioxide (CO_2), and nuclear waste disposal in underground structures. Fracture toughness, as a material property, is a crucial factor in the evaluation of the fracturing of brittle rock. The toughness of a rock is a measure of its ability to withstand fracturing. In other words, a rock with high toughness requires a substantial amount of energy to experience failure; a considerable amount of energy is absorbed by a rock with high toughness when it fractures. One of the most often used methods for determining the fracture toughness of rocks under confinement pressure is the burst experiment in the laboratory (Abou-Sayed, 1978). To perform this test, a hollowed-out cylindrical sample with two wing cracks is subjected to radial confinement on the boundary while a simultaneous interior pressure is applied. The inner and outer pressures (P_i and P_o) are increased proportionally until the sample bursts.

The burst experiment is carried out on a thick-walled cylindrical sample with axial bi-wing notches to simulate fracture initiation, and then the fracture toughness estimation procedures are followed. Bowie & Freese (1972) determined the stress intensity factor numerically at the crack tip using "modified mapping-collacation" technique. In their study, researchers benefit from the assumption of orienting the x and y axes in such a way that they coincide with the principle planes of elastic symmetry of the orthotropic plate, which enables them to simplify the constitutive equations. Under this assumption, an Airy stress function for plane symmetric loading defines the stress intensity factor. In the following years, Clifton et al. (1976) performed a series of experiments on various rock samples (sandstone, siltstone, and shale) to estimate fracture toughness, applying closed-form approximations of the stress intensity factor for simple geometries and load cases in addition to numerical simulations. These studies form the basis, respectively, for subsequent stress intensity factor and fracture toughness estimations in Abou-Sayed (1978).

Over the years, it has been found that the fracture toughness of rocks under confining pressure can be significantly increased compared to the laboratory results of unconfined testing.

Yoshioka et al. (2023) and Zhang (2019) have also carried out a series of burst experiments using different configurations to better understand crack propagation and fracture toughness estimation. Figure 1.1 illustrates a combination of published results that demonstrate a positive correlation between confining stress and fracture toughness.

However, Yoshioka et al. (2023) have numerically and experimentally demonstrated that the burst experiment may be essentially dependent on the confining stress in a way that is not considered in the analysis of the experimental data. They showed that the test configuration with stable manner allows researchers to detect the onset of crack propagation earlier, which leads to an overestimation of fracture toughness. Hence, it was demonstrated that more accurate fracture toughness estimation is possible with

unstable crack propagation, whereas the fracture toughness may be systematically overestimated in the original burst experiment configuration. This approach requires further investigation through additional experiments (with stable and unstable designs) to assess the feasibility and accuracy of the burst experiment. In other words, the accuracy and reliability of the burst experiment should be investigated in a more comprehensive manner. This thesis aims to improve both the feasibility and accuracy of the burst experiment test using numerical and experimental techniques to perform additional experiments with various configurations. Thus, a more accurate estimation of the fracture toughness is achieved.
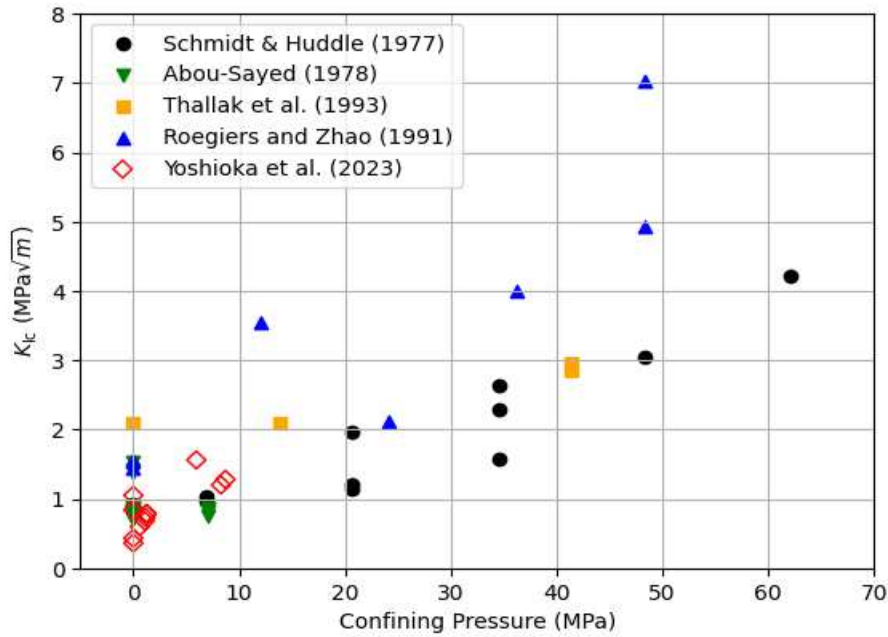
Figure 1.1: Fracture toughness vs confining pressure of Indiana Limestone (after Yoshioka et al., 2023)

1.1 Motivation

Rock fracture toughness has been measured using different experimental techniques, including the single-edge-notch test, the three-point-bending test, the confined cylindrical cell, the chevron-notched disk specimen (CDISK), and the beam test. These tests show a positive correlation between confining stress and fracture toughness. The burst experiment is the most popular laboratory test commonly applied in the oil and gas industry to estimate fracture toughness under confining pressure (Abou-Sayed, 1978). However, the recent studies of Yoshioka et al. (2023) and Zhang (2019) have analyzed the accuracy of this well-known test method and demonstrated some potential inaccuracies in the fracture toughness estimation. Yoshioka et al. (2023) have modified the current burst experiment configuration to have more accurate fracture toughness measurements. They have used the $G - \theta$ method to calculate the stress intensity factor numerically and set the experimental geometry and stress conditions such that the fractures occur in an "unstable" manner. During the laboratory tests, the acoustic emission monitoring method is implemented to demonstrate that stable crack propagation normally occurs well

before the final failure. This situation leads to an overestimation of fracture toughness when it is calculated using the peak pressure result according to the original test procedure. All these questions and recent developments related to the accuracy of burst experiments highlight the need to obtain more experimental data. In other words, the accuracy and reliability of the burst experiment should be investigated in a more comprehensive manner. In this sense, this thesis presents results from numerical and experimental simulations of the burst experiment. The numerical analysis method is used to calculate the stress intensity factor, applying different loading and geometrical configurations as an initial step to fracture toughness estimation. Eventually, a series of burst experiments are performed in the laboratory with different configurations, similar to recent studies, to assess the feasibility and accuracy of the facture toughness estimations on limestone samples under confining pressure. In some cases, acoustic emission monitoring is used to better understand crack growth mechanisms and to improve the accuracy of fracture toughness estimation with burst experiments.

1.2 Objectives

In recent years, the stability and reliability of this burst experiment testing method have been a matter of discussion in the rock mechanics community.

The primary objective is to analyze the reliability of burst experiments by implementing stable and unstable test configurations with specific combinations of sample geometry and loading conditions for the estimation of more accurate fracture toughness under confining pressure.

The second objective is to produce more accurate fracture toughness estimation results to compare both stable and unstable configuration results with the recent studies.

The third objective is to observe experimental behavior in both stable and unstable configurations. Some of the experiments are planned with acoustic emission monitoring to detect the actual onset of crack propagation.

The fourth objective is to investigate the effect of confining pressure on fracture toughness estimation in both fixed confinement and burst experiments.

2 Literature Review

Griffith (1921) conducted a sequence of experiments, analyzed stress, and integrated previous research in his exceptional paper to establish the fundamental concept that forms the basis of the contemporary theory of linear elastic fracture mechanics (LEFM). Griffith's energy relationship is founded upon the principles of linear elasticity theory, which predicts that stress at the tip of a sharp flaw in a linear elastic material is infinite. A few years later, he stated that a crack will propagate when the potential energy release rate (strain energy release rate) that occurs due to the crack growth is equal to or greater than the increase in surface energy due to the creation of new free surfaces (Figure 2.1) (Griffith, 1924). Although this theory is applicable to brittle materials such as glass fibers, the predicted surface energy is usually remarkably high, especially for ductile materials such as steel. It depends on a critical energy release rate, G_c, which is geometry-independent and thus a material property. When the application of load results solely in the initiation of the fracture, without any shearing or tearing occurring, and when material damage is localized to a very small region near the crack tip, the energy criterion is almost equivalent to $K_I = K_{IC}$. In other words, fracture occurs when $K_I = K_{IC}$ (Irwin, 1957), where K_I is computed as the stress intensity factor, and K_{IC} is the material fracture toughness. The critical energy release rate, G_c, can also be related to rock fracture toughness, K_{IC}, via Eq. (2.1):

$$G_c = \frac{K_{IC}^2}{E'} \tag{2.1}$$

where E' = E for plane stress and E' = E/(1-v^2) for plane strain, where E is the Young's modulus and v is the Poisson's ratio.
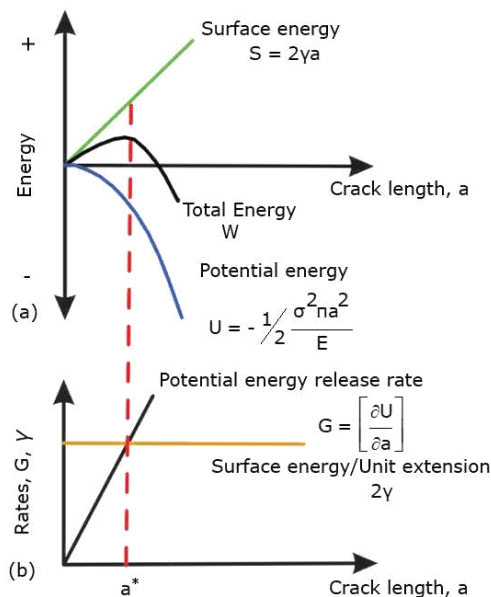
Figure 2.1: Diagram for the Griffith theory a) Variation of energy with crack length b) Variation of energy rates with crack length (a* is the critical Griffith crack length)

Crack growth conditions can be estimated based on LEFM by comparing the stress intensity factor against the measured fracture toughness of the material. Consequently, K_{IC} can be estimated through experiments utilizing the computed critical stress intensity factor taken at the time of crack propagation.

For rocks, it is observed that the K_{IC} depends on geometry and loading conditions, even though this is supposed to be a constant material property. For instance, Schmidtt & Huddler (1977) have investigated the effect of confinement on fracture toughness of Indiana Limestone. They have measured fracture toughness for 11 samples using two different laboratory experiment configurations, namely, a single-edge-notch and three-point-bend (Figure 2.2). They came to the conclusion that fracture toughness increases with increased confining pressure based on experimental data. A linear positive correlation was observed between the confining stress and the fracture toughness in the experiments having confining pressure range from 0 MPa to 62 MPa (see Figure 1.1).
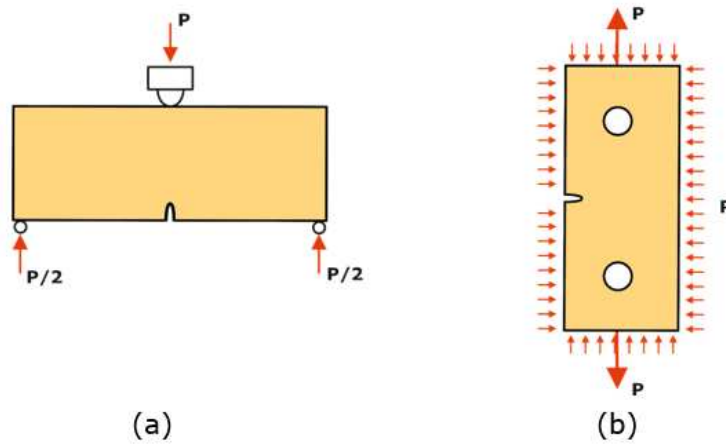
Figure 2.2: a) Three-point bend test; b) Single-edge test (after Schmidtt & Huddler, 1977)

As it was mentioned in the introduction, Abou-Sayed, (1978) has developed an experimental technique, namely, a burst experiment to measure rock fracture toughness considering in-situ downhole stress conditions and pore pressure (Figure 2.3). He has improved the burst test configuration for measuring K_{IC} under confining pressure by using a pressure chamber. The stress intensity factor was obtained by the principle of superposition, which considers non-dimensional stress intensity factors corresponding to the unjacketed (without applying confining pressure) and jacketed (sample subjected to confining pressure) burst experiment. Then, fracture toughness value under confining pressure, K_{IC}^{C}, was calculated using Eq.(2.2) below:

$$K_{IC}^{C} = \bar{P}_i \sqrt{\pi a}\, \bar{K}_I^{*c}$$
(2.2)

where $\bar{K}_I^{*c}$ is the non-dimensional stress intensity factor, which is depending on sample geometry, initial notch length and geometrical loading condition, $\bar{P}_i$ is internal pressure and a is the radius of the

borehole. The results showed that increased confining pressure leads to substantial increase in fracture toughness of Indiana Limestone (see Figure 1.1).
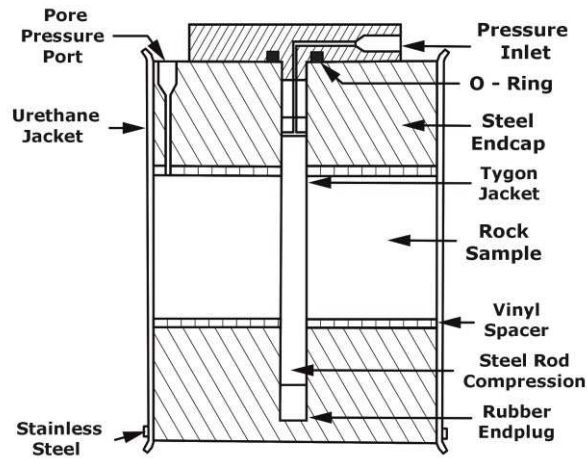
Figure 2.3: Schematic of burst test and sample cross-section (after Abou-Sayed, 1978)

Roegiers and Zhao (1991) carried out laboratory experiments to measure K_{IC} of rocks combining the influence of pressure and temperature for simulating reservoir conditions. They used Chevron -notched Brazilian Disk (CDISK) samples in their investigation. Stress intensity factory was estimated using the principle of superposition for their study (Figure 2.4).
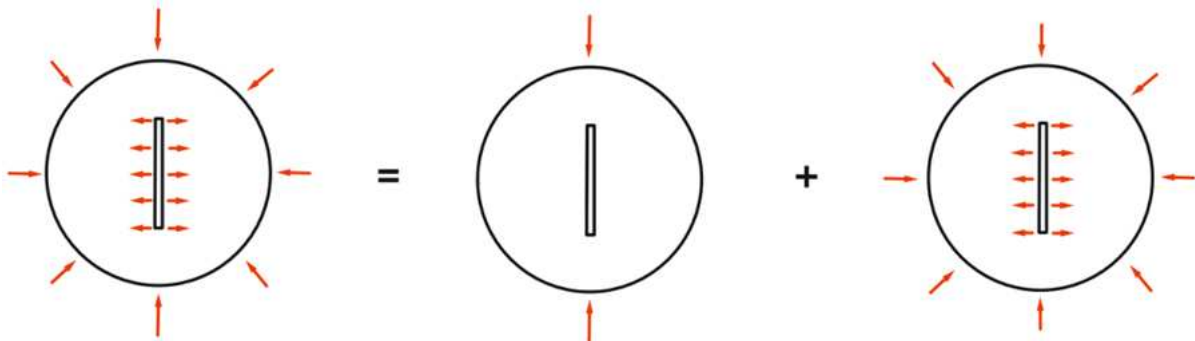
Figure 2.4: Superposition of stress intensity factors (after Roegiers & Zhao, 1991)

They developed a new load cell to measure K_{IC} of CDISK samples (Figure 2.5). In their test, P is the primary loading that is applied to the specimen, and the confining pressure is provided by hydraulic oil. According to the results of their experiments on chalk, limestone and sandstone samples, rock fracture toughness measurements show relatively higher values compared to similar studies in the literature. Furthermore, a significant increase of fracture toughness was observed with increasing confining stress similar to previous studies (Figure 1.1).
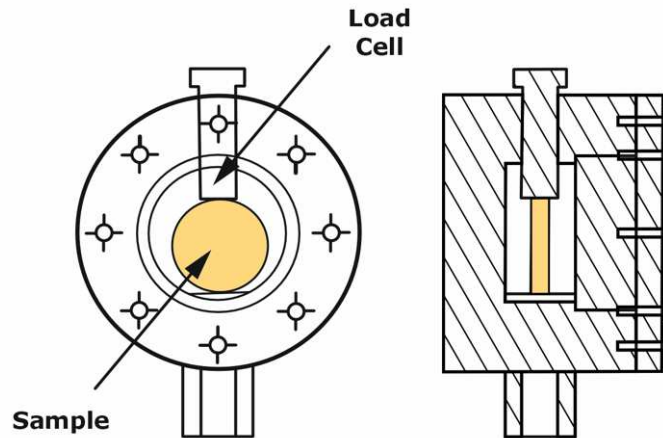
Figure 2.5: Load Cell Design (after Roegiers & Zhao, 1991)

Thallak et al., (1993) developed and performed several tests to measure fracture toughness in a setting similar to hydraulic fracturing. Figure 2.6 presents a schematic drawing of the test specimen configuration, wherein the specimen is placed inside a cylindrical cell, and fracture fluid is injected continuously until crack growth or fracture break-through is experienced. The fluid in the chamber provides confining pressure and sealing is provided by a membrane. The LEFM technique was used to measure fracture toughness of Sciota Sandstone and Indiana Limestone rock samples. A limited number of tests on Indiana limestone have yielded results that show a slightly higher hydrofracture toughness at zero pressure and a smaller variation with pressure compared to the Sciota Sandstone parameters (Figure 1.1).
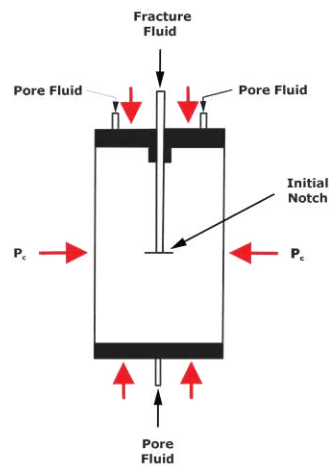
Figure 2.6: Laboratory test setup for hydraulic fracture test (after Thallak et al., 1993)

Ko and Kemeny (2007) analyzed the influences of confining pressure and loading rate on the fracture toughness by running a short beam compression test on Flagstaff Sandstone. The testing apparatus of short beam test is illustrated in Figure 2.7. A loading platen is used to apply compression to the top of the specimen and the confining pressure is provided by the surrounding cell. They showed the best-fit

regression line based on fracture toughness versus confining pressure and loading rate. The fracture toughness was observed to escalate as the confining pressure and loading rate increase.
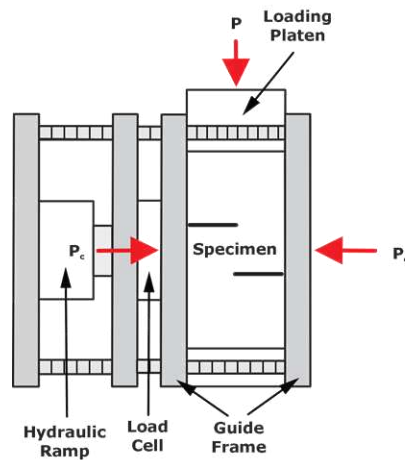
Figure 2.7: Testing apparatus of short beam compression test (after Ko & Kemeny, 2007)

Yoshioka et al. (2023) focused on examining the crack stability in the burst experiment. Through their study, they proposed certain modifications to the experimental design that enhance the growth of unstable fracture. The challenge in interpreting the situation arises due to the potential inaccuracy of assuming that the burst pressure, P_{ic}, always provides the necessary load for the initial extension of a crack with a given length, L. If there is a consistent propagation of cracks before the sudden change in pressure, resulting in an eventual unstable "burst", the length of the crack L will be greater at the moment of the burst occurrence compared to L in the Figure 2.8, which is assumed for the analysis.
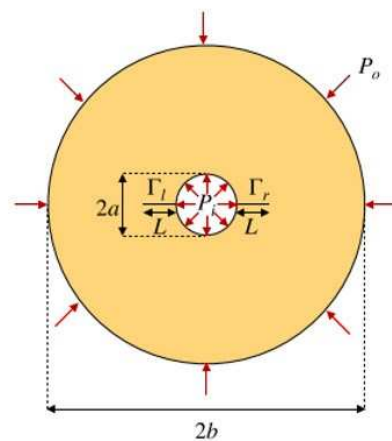
Figure 2.8: Schematic of the burst experiment (after Yoshioka et al., 2023)

This will result in overestimating the fracture toughness and hence overstating the dependence of fracture toughness on confinement. To this point, there are three possible evolutions of K_I^{B*} (details given in Section 3.3) and the corresponding P_{ic}, which can be applied to determine the stability of crack growth in the burst experiment. Therefore, it is aimed to contribute to reducing the ambiguity associated

with interpreting the critical pressure through these modifications. The researchers propose the following suggestions as a result of their investigation. It is desirable for the geometry and loading conditions to be designed in a way that promotes unstable crack propagation. In other words, the stress intensity factor or elastic energy release rate should be a decreasing function at the initial crack length. If the crack propagation remains stable in the selected initial geometry, it might be feasible to identify the initiation of crack propagation by employing acoustic emission monitoring, although at the cost of reduced accuracy.

3 Theoretical Background

3.1 Problem Statement

Think of a cylinder rock sample placed in the center of a burst cell. There are diametrically opposed initial notches along the central borehole. The confining pressure, P_o, is applied to the outside surface of the sample, while the inner pressure, P_i, is applied inside the borehole (recall Figure 2.8).

At the beginning of the burst experiment, the pressure is increased simultaneously and proportionally, with the ratio of the outer pressure to inner pressure remaining constant, until a pressure drop is observed and the sample bursts. The pressure data is recorded, and eventually the peak pressure is chosen to estimate the fracture toughness. Figure 3.1 shows the burst experimental setup with the application of pressures.
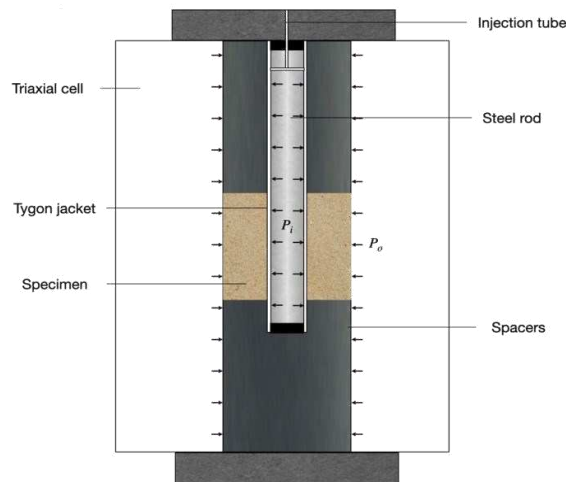
Figure 3.1: The burst experiment setup and application of pressures (Yoshioka et al., 2023)

3.2 Fracture Toughness Estimation

In the mid-1950s, Irwin and his associates developed a modified version of Griffith's method, restructuring it to focus on stress instead of energy. They developed the stress intensity factor, which is one of the most fundamental and useful parameters in all fracture mechanics (Erdogan, 2000). The stress intensity factor (K_I) is defined as the stress state at a crack tip in fracture mechanics. The stress intensity factor for a straight crack having a length of 2a in an infinite plane with a uniform stress field σ is given in Eq. (3.1):

$$K_I = \sigma\sqrt{\pi a} \qquad (3.1)$$
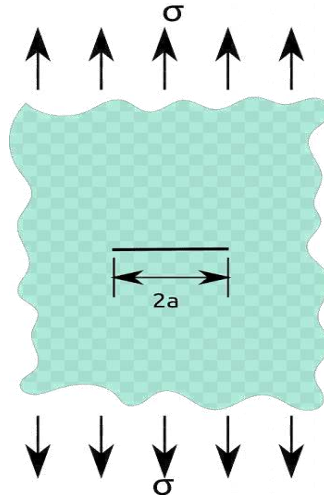
Figure 3.2: Crack in an infinite plate under mode I loading (URL-1)

The critical value of the stress intensity factor at which the crack propagates is called the fracture toughness, denoted K_{IC}. When we focus on the development of K_I in relation to the length of fracture, K_I (a, b, l_0, P_o, P_i) will be the stress intensity factor associated with a sample with an inner radius of a, an outer radius of b, an initial fracture length of l_0, and inner and outer pressures, respectively, P_o and P_i. Hence, K_I is not an intrinsic property of rock, but rather depends on these testing conditions. After conducting the experiment and determining the critical pressure related to crack growth, the fracture toughness K_{IC} for each test can be estimated by employing the equation proposed by Abou-Sayed, (1978), which is expressed as:

$$K_{IC}(\ell) = P_{ic} K_I^{B*}(1, w, \ell, p*)\sqrt{a\pi} \tag{3.2}$$

Here P_{ic} is the internal pressure at the time of the burst. Also, K_I^{B*} is the normalized stress intensity factor for a unit internal pressure, which can be computed numerically as a function of w, ℓ, and p^*. Where w, ℓ, p^* are three non-dimensional parameters:

$$w = \frac{b}{a} \quad p* = \frac{P_o}{P_i} \quad \ell = \frac{l_0}{b-a} \tag{3.3}$$

The ratio of the outer pressure to the inner pressure is p^*, and the ratio of the outer radius to the inner radius is w. Normalized crack length is ℓ, where l_0 is the initial length of the notch.

3.3 Fracture Propagation and Global Stability Criterion

The burst experiment was designed to estimate the resistance to fracturing K_{IC} (also known as fracture toughness) of rock samples having two notches of length l_0. This estimation is conducted under varying confining pressures, The main challenge in estimating pressure-dependent fracture toughness is that the tensile failure is induced in a sample subjected to compression. Over the execution of burst experiment, the confining and inner pressures are increased simultaneously and proportionally with a constant ratio

of p^*, until the sample ruptures. During the experiment, different regimes of crack growth are observed, namely stable and unstable. The calculation of these regimes depends on factors such as the confining pressure and geometry. When it comes to unstable crack propagation, the phase-field models for hydraulic fracturing do not provide relevant information (Tanné, 2017). Instead, we employ a stress intensity factor (SIF) analysis along the fracture path to ascertain the stability regimes of crack growth. In more recent studies, researchers have examined stable and unstable crack growth regimes, associating inner pressure, P_{ic}, with stress intensity factor analysis (Yoshioka et al., 2023); (Huang et al., 2022).

The challenge in interpretation arises from the potential inaccuracy of assuming that the burst pressure, P_{ic}, provides the necessary loading for the initial extension of a crack with a length of l_0. If there is stable crack growth prior to the sudden change in pressure, leading to an eventual unstable "burst", the actual length of the crack at the time of burst will be greater than what is predicted by the analysis. This will result in overestimating the fracture toughness and, hence, overstating the dependence of fracture toughness on confinement. At this stage, three potential variations of K_I^{B*} and the corresponding P_{ic} exist, which can be utilized to determine the stability of crack growth in the burst experiment (Huang et al., 2022).

(a) The K_I^{B*} experiences a steady decrease with the fracture length, ℓ, increasing, while the P_{ic} is an increasing function of ℓ (Figure 3.3a). This case leads to "stable" crack growth in the burst experiment.

(b) The K_I^{B*} shows a fluctuation at the beginning and then increases with ℓ increasing, while the P_{ic} also shows a fluctuation initially and then decreases with ℓ increasing (see Figure 3.3b). The crack growth will exist either stably or unstably, depending on the normalized crack length ℓ.

(c) The K_I^{B*} increases monotonically with ℓ increasing, while the P_{ic} decreases with ℓ increasing monotonically (Figure 3.3c). In this case, unstable crack growth is observed, so the sample will burst instantaneously due to the dynamic propagation.
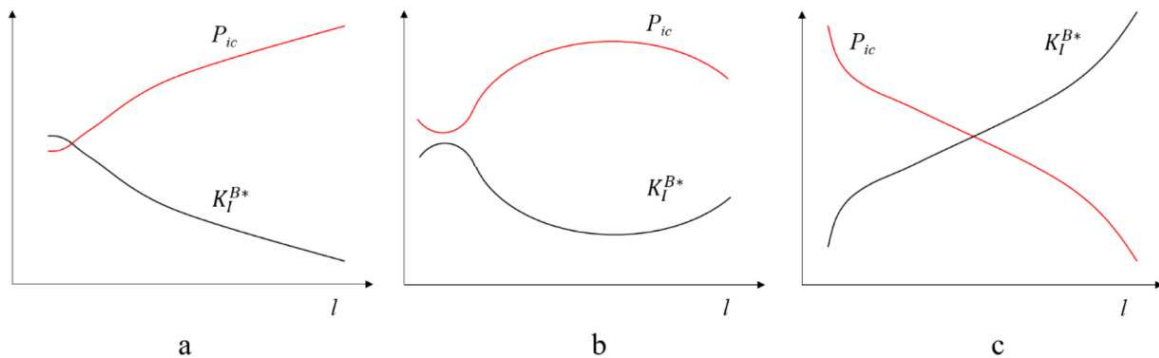
Figure 3.3: Evaluation of crack growth stability regimes (Huang et al., 2022)

3.4 SIF Calculation

The calculation of SIF is a significant step to show the influence of the test configuration, loads, and crack length upon the stresses near the end of the crack in brittle tensile fracture mechanics (Irwin, 1957). The simulation of burst SIF is a crucial step in the estimation of fracture toughness. Throughout this procedure, SIF is computed numerically using the $G - \theta$ method. In comparison to the J-integral technique, the $G - \theta$ method offers an alternative approach to determining the energy release rate in elastic, viscoplastic, or dynamic fractures. This method utilizes a surface integral, allowing for the determination of the energy release rate with a reasonable computational effort (Dubois et al., 1999).

When we consider the evolution of the stress intensity factor $K_I^{B^*}(w, \ell, p^*)$ with the crack length ℓ for the parameter analysis (w, p^*) in order to investigate the stability of crack propagation regimes, the burst problem denoted (B) is decomposed into the elementary problems applying LEFM. Abou-Sayed (1978) proposed an approach to decompose it into two problems following Figure 3.4 a situation where pressure is applied only to the inner cylinder, known as the jacketed problem (J), and the unjacketed problem (U) where the fluid exerts pressure on all internal sides. In this case, burst SIF is calculated as the sum of the jacketed SIF and the unjacketed SIF follows:

$$K_I^{B^*}(w, \ell, p*) = K_I^{J^*}(w, \ell) - p * K_I^{U^*}(w, \ell) \tag{3.4}$$

where $K_I^{U^*}(w, \ell) \geq 0$ for a positive P_o applied in the interior of the geometry.
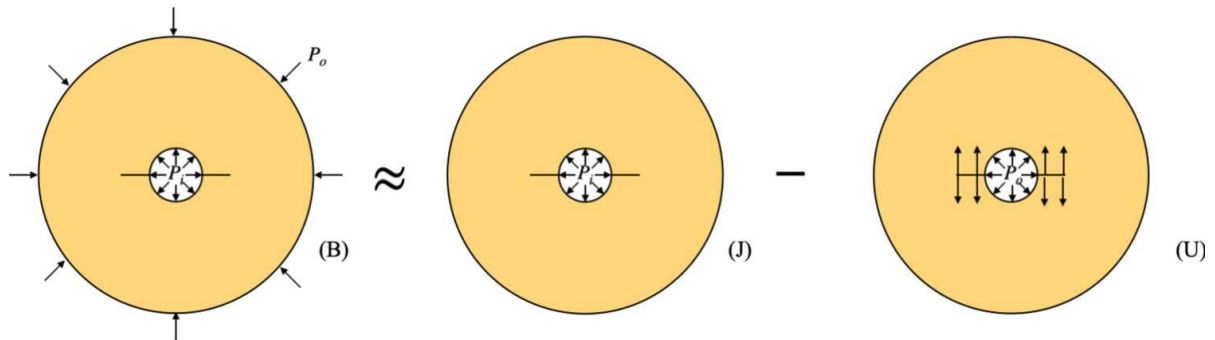
Figure 3.4: Superposition of the burst problem approximated in Abou-Sayed (1978) (Yoshioka et al., 2023)

However, in this study, the burst problem is decomposed into two problems following Tanné (2017): the superposition of jacketed test (J) and a constrained test (C), as illustrated in Figure 3.5 for a unit internal pressure. Similar to Abou-Sayed (1978), the pressure is applied only in the inner cylinder for the jacketed problem (J), whereas a constrained problem has only a confining pressure applied on the outer cylinder named (C). Hence, the burst SIF for (B) can then be expressed as the sum of the jacketed SIF (J) and the constrained SIF (C):

$$K_I^{B^*}(w, \ell, p*) = K_I^{J^*}(w, \ell) + p * K_I^{C^*}(w, \ell) \tag{3.5}$$

where $K_I^{C^*}(w, \ell)$ is positive for negative applied external pressure P_o.
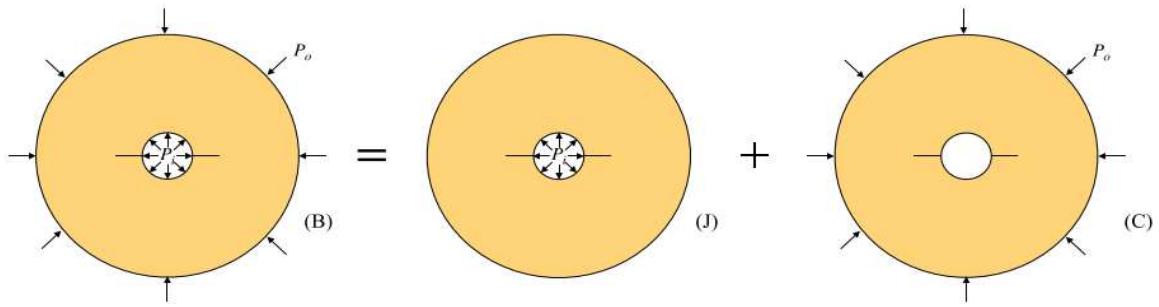
Figure 3.5: Decomposition of burst problem (B) into jacketed (J) and constrained (C) problems according to Tanné (2017) (Yoshioka et al., 2023)

Tanné (2017) decomposition does not consider pore pressure (P_p) within the sample, as a drain is employed to release the internal pressure within the rock.

In Figure 3.6, the results of $K_I^{J^*}$ and $K_I^{U^*}$ computation applying the G − θ method are closely aligned with the values reported by Clifton et al. (1976), indicating a strong agreement between the two sets of data. The G – θ approach is a calculation of the second derivatives of the potential energy concerning the crack length, achieved by implementing a virtual perturbation of the domain (vector θ) in the direction of crack propagation (Destuynder et al., 1981; Suo & Combescure, 1992). Then, the SIF is calculated using the Irwin formula (Equation(2.1)) based on the computed G.
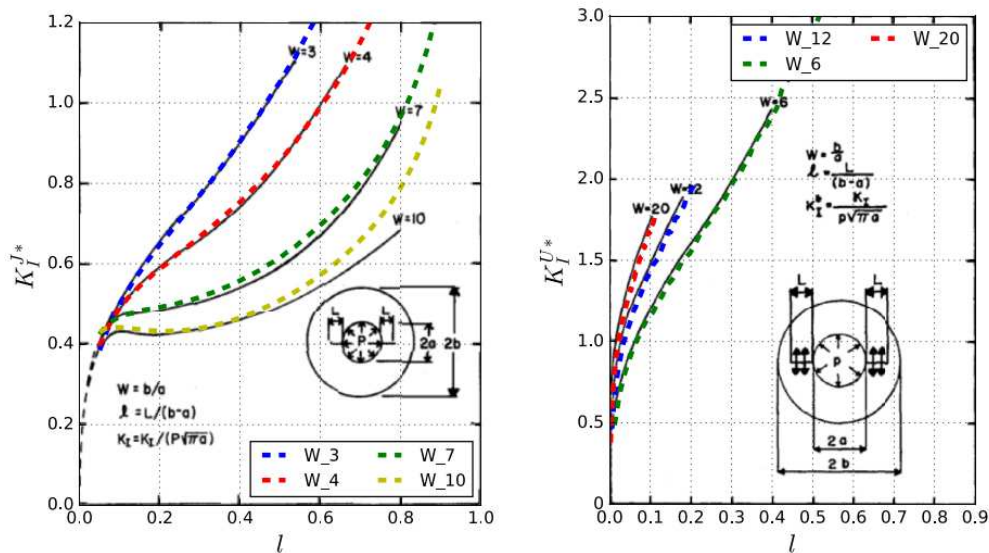
Figure 3.6: Comparison of computed SIF evolution for the jacketed and unjacketed problems vs. normalized crack length ℓ with Clifton et al. (1976). Colored lines numerical SIF computation results based on G – θ method (Yoshioka et al., 2023)

3.4.1 Numerical Simulation

Numerical simulation of the burst experiment enables researchers to compute SIF using the $G - \theta$ method, which is beneficial compared to alternative methods. For this reason, a quarter model of the burst experiment has been simulated using OpenGeoSys (OGS), which is an open-source project for the development of numerical applications for the simulation of coupled thermo-hydro-mechanical-chemical (THMC) processes in porous and fractured media (URL-2).

The material behavior, model geometry, notch length, number of notches, loading and boundary conditions, and meshing have crucial roles in the quality of simulation results. The simulation strategy focuses on generating a tensile deformation at the crack tip for various configurations to calculate SIF. Figure 3.7 shows the schematic structure of the model, which is described in detail below. The geometry and meshing of the model were generated via Gmsh, which is an open-source 3D finite element mesh generator with a built-in CAD engine and post-processor (URL-3). A quarter-burst experiment model was simulated using the symmetric modeling technique (Yoshioka et al., 2023). This quarter model was simulated for seven different outer and inner radius ratios ($w = 3$, $w = 4$, $w = 6$, $w = 7$, $w = 10$, $w = 12$, and $w = 20$) and the results were validated with Clifton et al. (1976) (recall Figure 3.6). Following this, fifty different notch lengths were simulated in different models on the horizontal axis. Eventually, within the scope of this thesis, G and SIF values for $w = 3$ and $w = 12$ configurations were computed, and the results were presented graphically by comparing them with normalized notch length in Section 3.4.2. Fine meshing was used along the notch on the horizontal axis to obtain more reliable results.
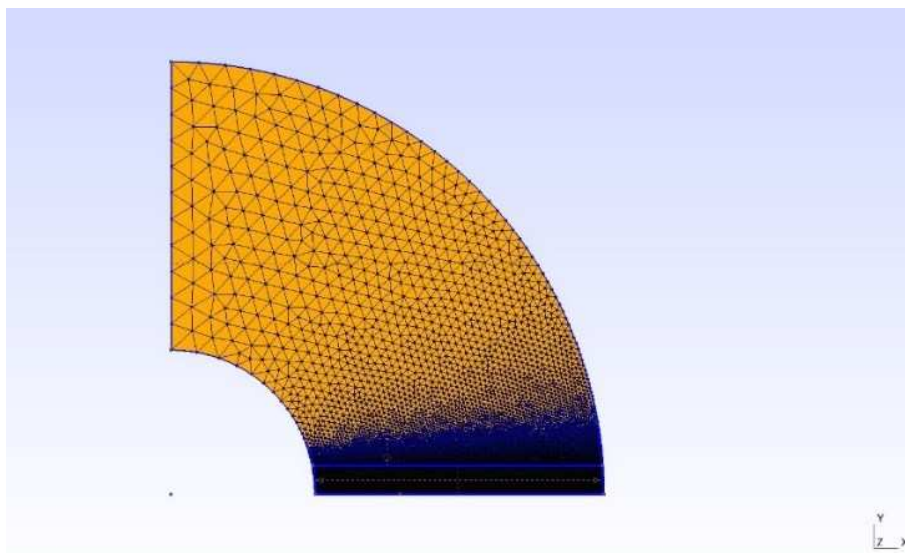
Figure 3.7: Principal sketch of the quarter model geometry and meshing in Gmsh

Jacketed (J) and constrained (C) approaches were computed in accordance with the decomposed burst problem according to Tanné (2017) to obtain SIF results (explained in detail in Section 3.4). The models were simulated based on linear elastic material behavior and run using OGS. Then, the results were

displayed and analyzed in ParaView, which is also an open-source platform to visualize and analyze modeling results. To simulate jacketed and constrained problems, inner and outer pressures are applied to the model, respectively. Restraint boundary conditions were applied on the horizontal axis immediately after the notch and on the vertical axis. No boundary restriction was applied to the outer surface boundary in jacketed cases where internal pressure was applied, while the inner surface boundary was not restrained in the constrained problem where external pressure was applied. Figure 3.8 illustrates example results in ParaView for both jacketed and constrained cases with applied boundary conditions on a model having displacement in X and Y directions.

(a)

(b)

(c)

(d)
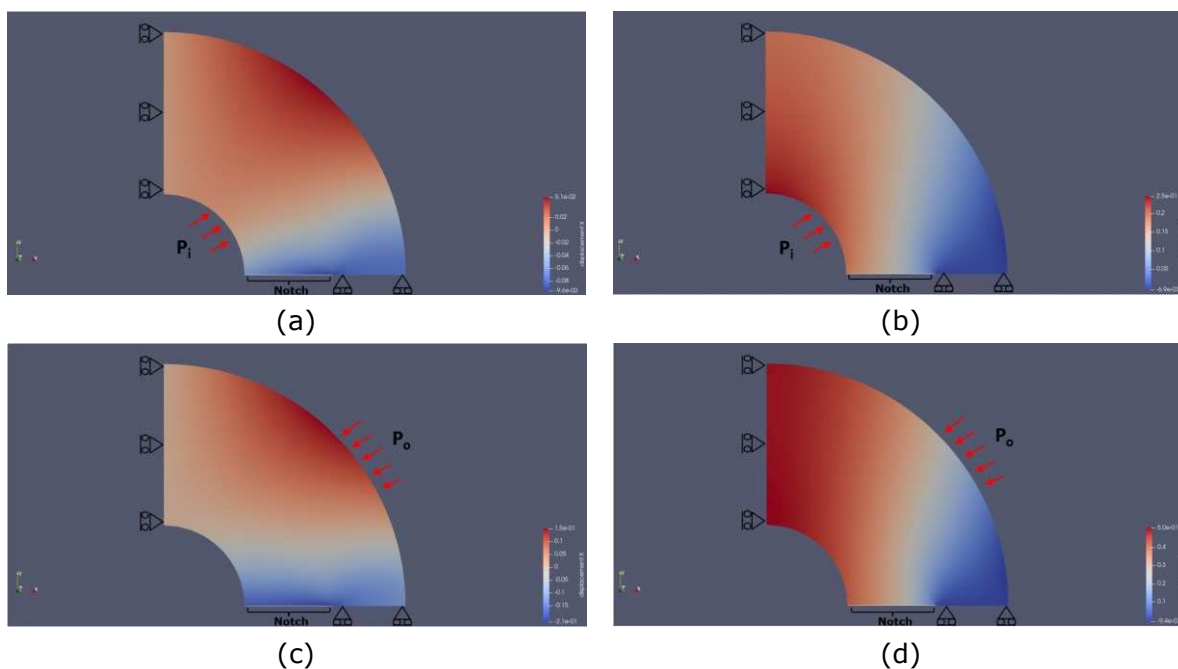
Figure 3.8: Restrain boundary and loading conditions for jacketed and constrained problems, (a) Jacketed case displaced in X direction (b) Jacketed case displaced in Y direction (c) Constrained case displaced in X direction (d) Constrained case displaced in Y direction

3.4.2 SIF Results

The SIFs of both jacketed (J) and constrained (C) problems were calculated numerically for $w = 3$ and $w = 12$ configurations using the $G - \theta$ method as mentioned in Section 3.4. The results from the superposition of these two SIFs vs. the normalized notch length ℓ are shown in Figure 3.9-10. Furthermore, SIFs were computed and are shown in Figure 3.11-12 for fixed confinement experiments, also having $w = 3$ and $w = 12$ configurations. In these simulation results, the four types of relationships between normalized SIF and normalized notch length ℓ are shown. According to these results, the stability of the crack growth can be interpreted based on the global stability criterion given in Figure 3.3. When K_I^{B*} shows an upward trend with increasing normalized notch length ℓ, unstable crack growth is expected. K_I^{B*} increases generally in direct proportion to the initial notch length. If K_I^{B*} shows a

downward trend with increasing normalized fracture length ℓ, it is possible to expect pre-existing stable crack growth according to our hypothesis. In general, it can be seen that the K_I^{B*} shows an increasing trend for all pressure ratios with $w = 3$ configuration (Figure 3.9), which means that the crack is supposed to grow unstably. However, K_I^{B*} shows a decreasing trend for almost all pressure ratios except for the unconfined case with $w = 12$ configuration (Figure 3.10), which means stable crack growth is expected for most of the cases prior to the rupture of sample. Like the simulation results of proportional pressure tests, for fixed confinement tests mainly unstable crack growth is expected with $w = 3$ configuration (Figure 3.11), whereas there is a stable crack growth with $w = 12$ configuration (Figure 3.12).

In order to calculate the fracture toughness with the SIF simulation, the dimensionless initial notch length l_0 is fixed to 7.62 mm, which corresponds to $\ell = 0.11$ for $w = 12$ and $\ell = 0.15$ for $w = 3$. Thus, the normalized value of K_I^{B*} can be calculated for each test considering the intended value of $p*$ and w on the computation results as shown in Figure 3.9-12. K_{IC} can be estimated for each case based on these values and Equation (3.2), when the critical inner pressure, P_{ic}, is known at the point of rupture after each burst experiment.
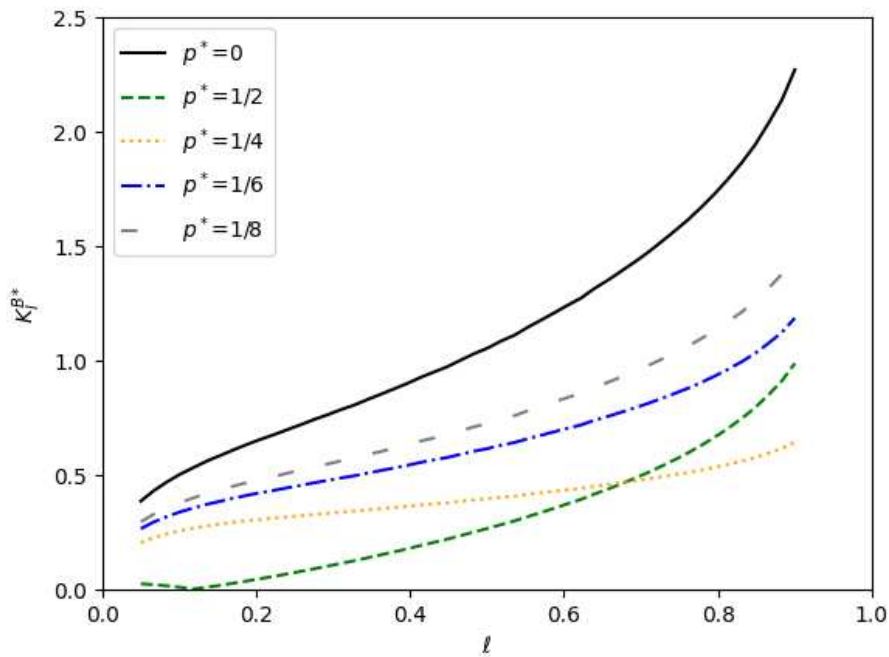
Figure 3.9: Simulation results of K_I^{B*} for $w = 3$
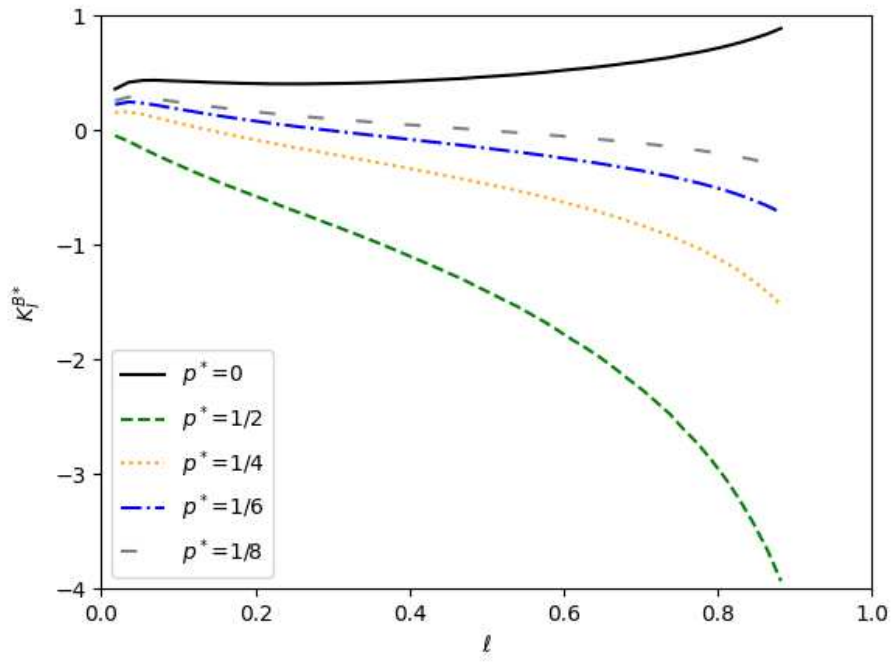
Figure 3.10: Simulation results of K_I^{B*} for $w = 12$
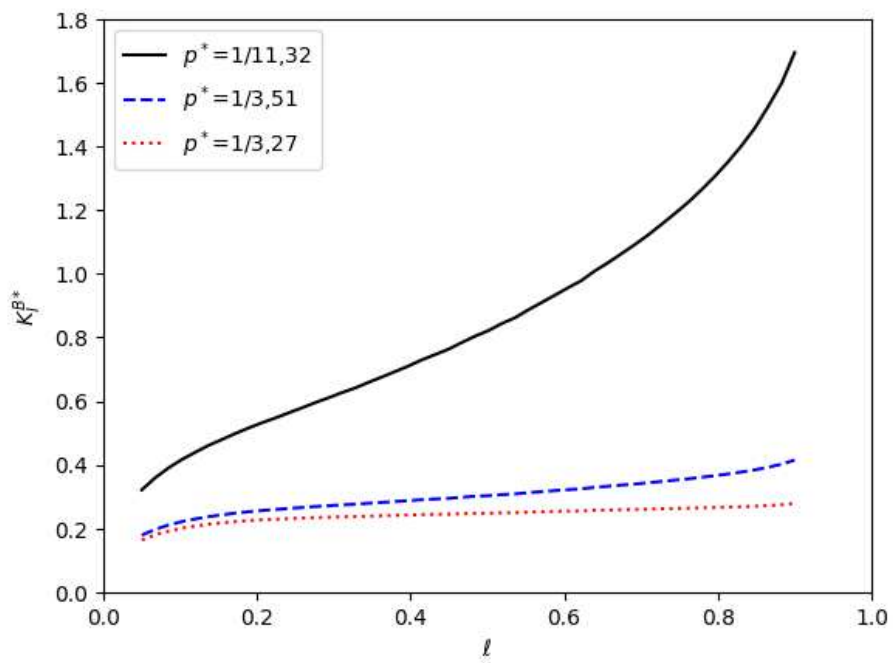
Figure 3.11: Simulation results of K_I^{B*} for fixed confinement tests with $w = 3$
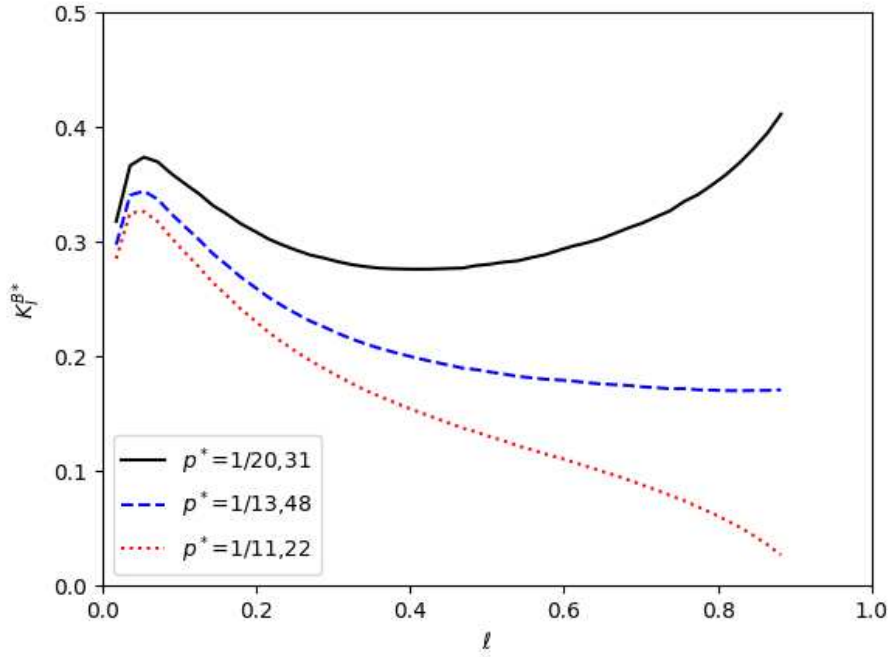
Figure 3.12: Simulation results of K_I^{B*} for fixed confinement tests with $w = 12$

4 Experimental Setup

4.1 Apparatus and Design Configurations

The main component of the burst experiment is a burst cell, which is surrounded by an oil-filled chamber providing the confining stress. The setup for the burst experiment can be seen in Figure 4.1. The initial step in conducting a test involves placing the cylindrical rock sample at the center of a burst cell, which is surrounded by an oil-filled chamber to apply the confining pressure. There is an outer membrane that acts as a barrier and effectively prevents the infiltration of oil into the chamber. The sample is positioned at the vertical midpoint of the chamber using a pair of aluminum spacers (Figure 4.2a). A tygon tube, as shown in Figure 4.2b, is inserted into the central hole of the sample, and sealed by two rubber plugs from top and bottom. The steel rod inside the tygon tube serves to keep the two rubber plugs in position, allowing them to expand by means of compression and thus improving the seal. This system allows for the application of internal pressure while simultaneously preventing the infiltration of fluid into the specimen. The internal pressure is applied by water, unlike the confinement pressure. The steel plate covers are secured in place using bolts at both the top and bottom to maintain the structural integrity of the system. Two ISCO syringe pumps are operated simultaneously to raise the inner pressure and the confining pressure proportionally until a pressure drop is observed.
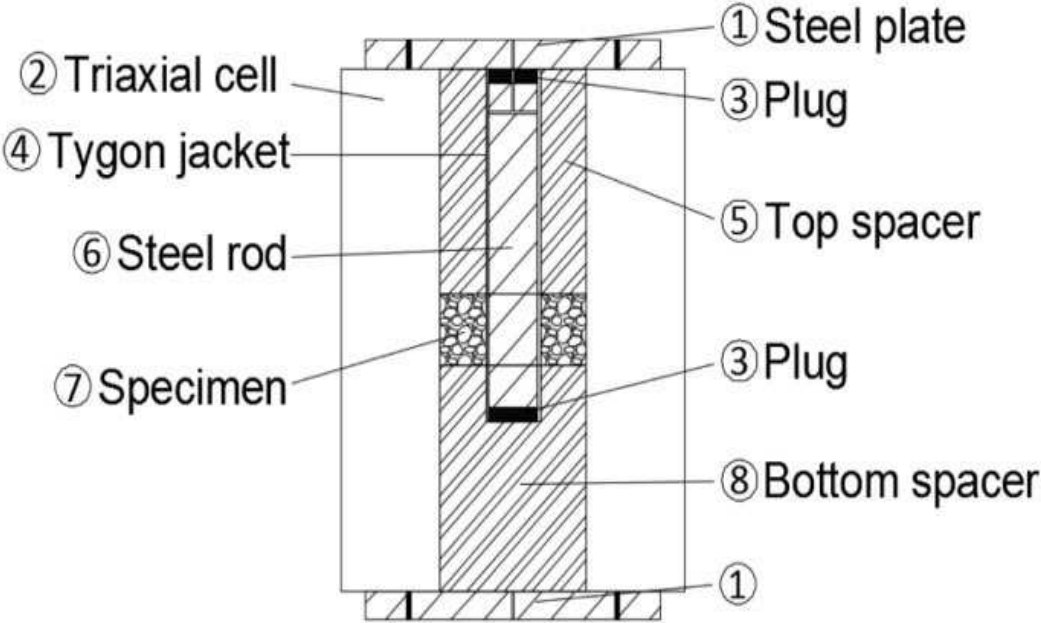
(a)
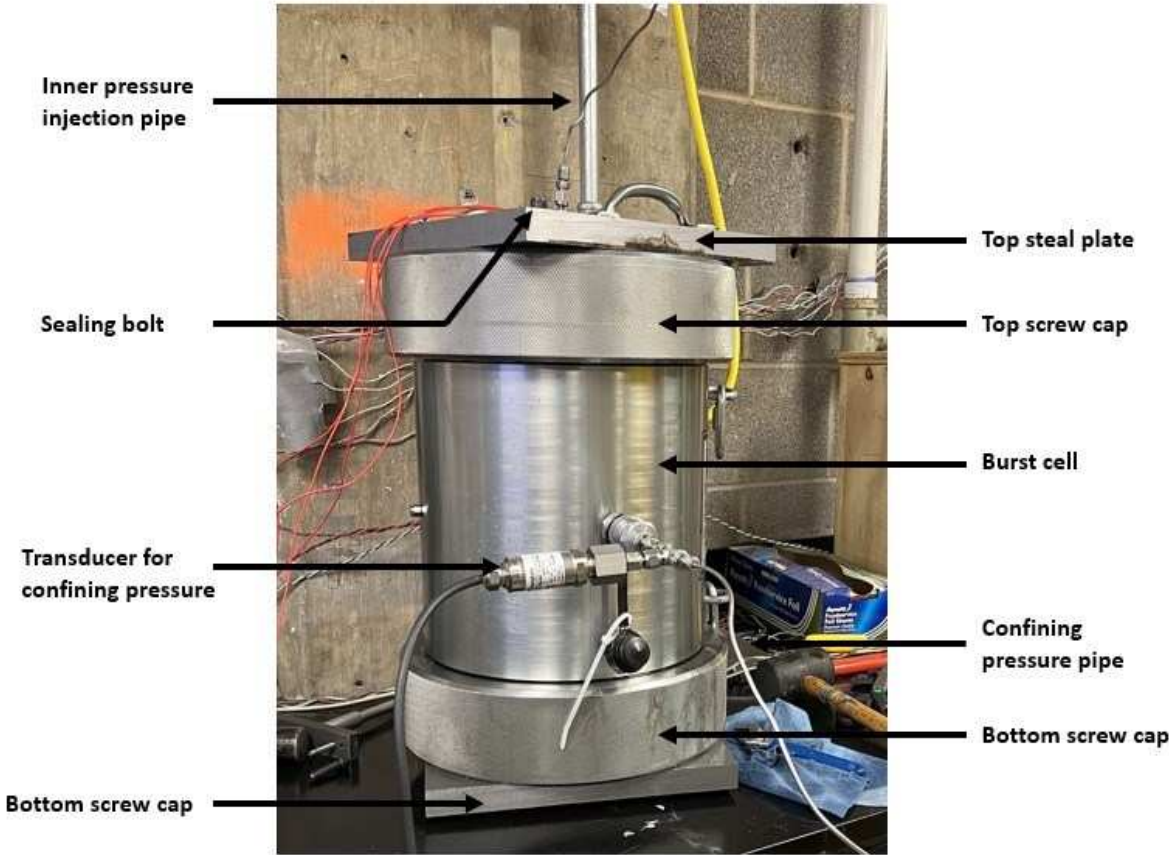
(b)

Figure 4.1: a) Apparatus design for burst experiment (afterAbou-Sayed, 1978) b) Burst cell

(a)

(b)
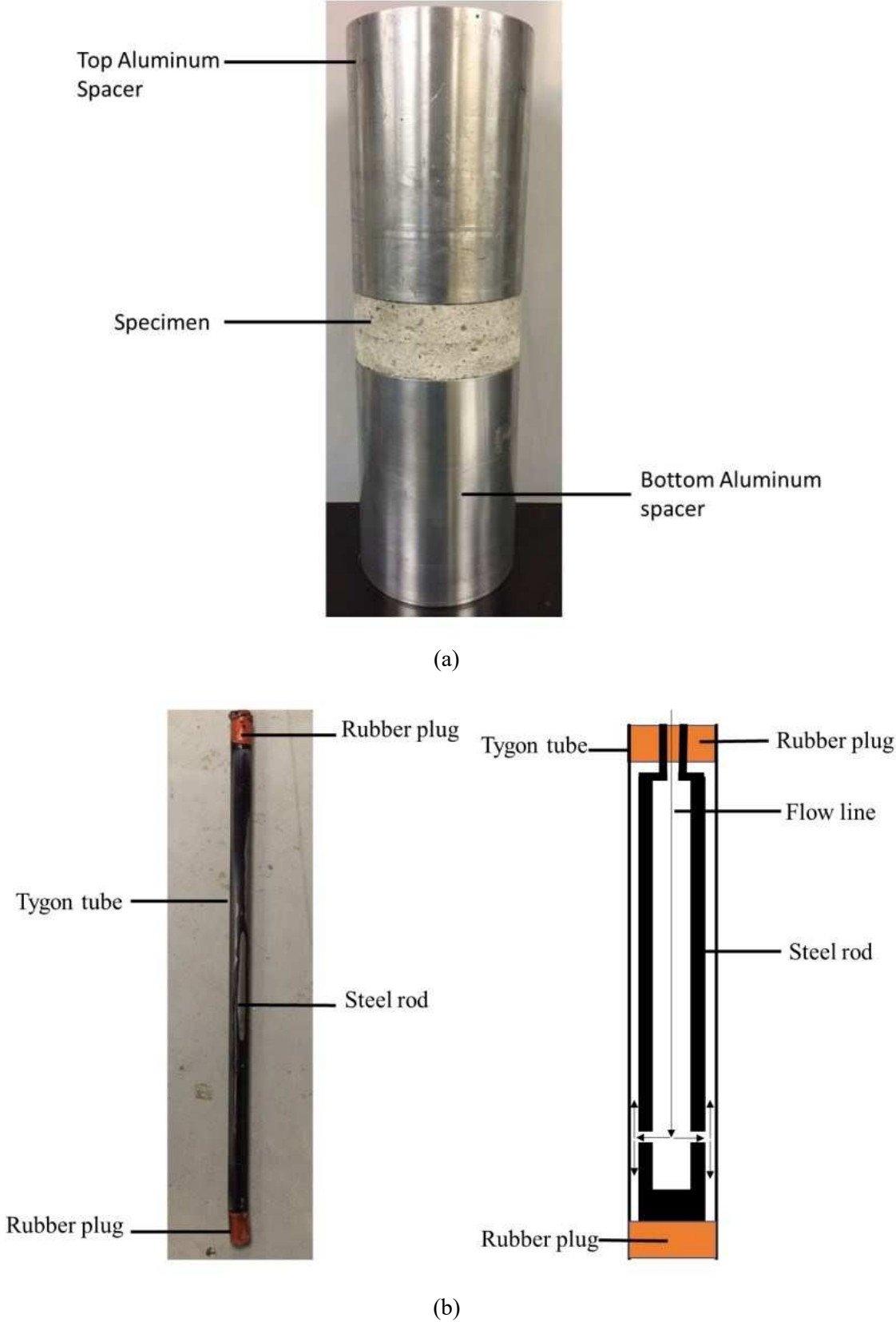
Figure 4.2: (a) Spacers and sample for tests b) Tygon tube to apply inner pressure and rubber plug for system sealing (Zhang, 2019)

The proposed design of the burst experiments is shown for the original burst experiment with proportional pressure ratios and fixed confinement configuration in Table 4.1 and Table 4.2, respectively. There are two different inner hole diameters: 12.7 mm ($w = 12$) and 50.8 mm ($w = 3$). The outer and inner pressure ratios are set to be 0, 1/6, and 1/8. The stability is assigned based on the global stability criterion explained in Section 3.3.

Table 4.1: Design of burst experiment configuration (the "Stability" column is a prediction based on the global stability criterion (see Section 3.3))

Test Name	Stability	Hole Diameter (mm)	w (b/a)	p^* (P_o/P_i)	p^*w
1, AE	unstable	12.7	12	0	0
2, AE	stable	12.7	12	1/8	1.5
3, AE	stable	12.7	12	1/6	2
4	unstable	50.8	3	0	0
5, AE	unstable	50.8	3	1/8	0.375
6, AE	unstable	50.8	3	1/6	0.5
7	unstable	50.8	3	1/6	0.5

Table 4.2: Design of fixed confinement test configuration (the "Stability" column is a prediction based on the global stability criterion (see Section 3.3))

Test Name	Stability	Fixed (P_o)	w (b/a)	p^* (P_o/P_i)	p^*w
F-1	Stable /Unstable	1	12	0.05	0.60
F-2, AE	Stable	3	12	0.07	0.89
F-3, AE	Stable	4.8	12	0.09	1.07
F-4	Unstable	0.5	3	0.09	0.27
F-5	Unstable	3.5	3	0.27	0.86
F-6	Unstable	6.5	3	0.31	0.92

4.2 Sample Preparation

Kasota Valley Limestone was used in the course of these experiments, which is a dolomitic limestone found and quarried in southern Minnesota, especially near the Minnesota River and its tributaries. Table 4.3 displays the measured rock properties of this limestone in the laboratory (G. Lu et al., 2020; Q. Lu et al., 2018).

Table 4.3: Material properties of Kasota Valley Limestone

Material property		Testing method
Young's modulus (GPa)	45	Uniaxial compression on cylindrical specimens (ASTME111-04, 2010a)
Poisson's ratio	0.3	Uniaxial compression on cylindrical specimens (ASTME132-04, 2010b)
Fracture toughness ($MPa\sqrt{m}$)	0.77	Three-point bending test on semicircular specimens (Kuruppu et al., 2014)

The sample preparation process began by cutting 152.4x152.4x152.4 mm cube samples (Figure 4.3a) into half on a water saw (Figure 4.3b). Afterwards, it was cut into a cylindrical shape with an outer diameter of 152.4 mm in the core drill. These were then again core drilled to give either a 12.7 mm or 50.8 mm diameter central hole (Figure 4.3c). Following this, surface grinding (Figure 4.3d) was applied until 63.5 mm thick samples were achieved with a parallel and flat surface. Lastly, a wire saw (as illustrated in Figure 4.3e) was utilized to cut two diametrically opposed (bi-wing) notches, each with a length of 7.62 mm. The eventual shape of the prepared samples with two different inner diameter is given in Figure 4.4.

(a)   (b)

(c)

(d)

(e)
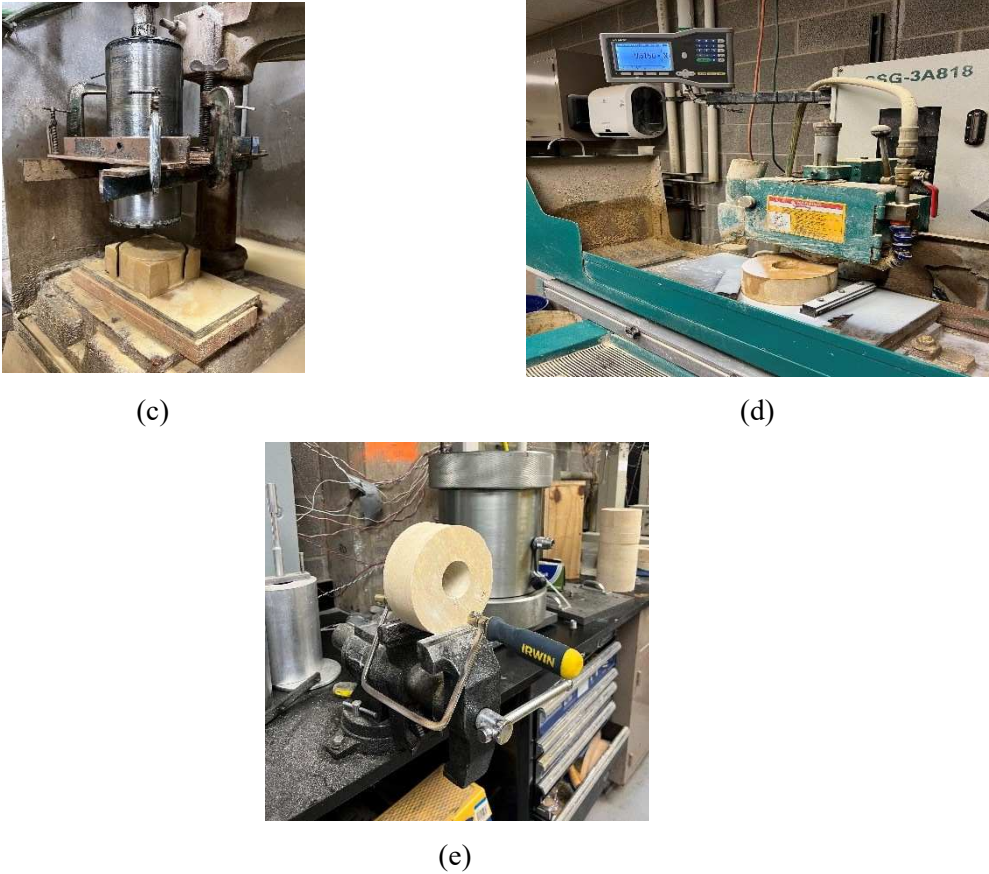
Figure 4.3: a) Cube sample, b) Water saw, c) Core drilling, d) Grinding machine, e) Wire saw

(a)

(b)

Figure 4.4: a) Limestone sample with 50.8 mm inner hole diameter b) Limestone sample with 12.7 mm inner hole diameter

4.3 Burst Experiment Procedure

The experimental setup necessitates substantial modifications when changing the radius ratio parameter, w. Therefore, we specifically focus on two values: $w = 12$ (with a 12.7 mm central hole) and $w = 3$ (with

a 50.8 mm central hole). The experimental setups involve the utilization of configurations that are either stable or unstable in alignment with the global stability criterion described in Section 3.3. Stable configurations use a 12.7 mm central hole ($w = 12$) with pressure ratios $p* = 1/8$ and $1/6$, whereas unstable configurations use a 12.7 mm central hole ($w = 12$) with $p* = 0$ and a 50.8 mm central hole ($w = 3$) with $p* = 0$, $1/8$, and $1/6$.

Initially, an aluminum spacer was placed at the base of the burst cell, followed by the placement of a tygon tube immediately (recall Figure 4.2) with a steel rod inside below the center hole. After that, the limestone sample and a second aluminum spacer were put inside the burst cell around the tygon tube. The sealing of the system was achieved by placing a steel plate on the top of the cell, and the top rubber plug was precisely located within this plate to generate effective sealing. The connection of two ISCO syringe pumps was established, whereby one pump was connected to the burst cell to apply confining pressure, and the other pump was connected to the central tube to provide the inner pressure.

After completing all the necessary preparations, the two ISCO syringe pumps were turned on simultaneously and set to pressure ramp rates to maintain a consistent ratio between the two pressures. The pressure and flow rate levels were continuously monitored until a sudden decrease in pressure or rise in flow rate was experienced.

4.4 Accoustic Emission Monitoring

Yoshioka et al. (2023) proposed that the pressure peak signifies the ultimate failure of the sample rather than the initial crack propagation, when crack propagation is stable at the onset. This situation leads to severely overestimating fracture toughness. They have also pointed out that it might be possible to detect the onset of crack propagation through acoustic emission monitoring, although at the cost of reduced accuracy. Therefore, an acoustic emission (AE) monitoring system has also been applied in this study to show evidence of crack propagation well before rupturing the sample (Figure 4.5a).

Because of limitations in access within the burst cell, four sensors were strategically placed on the bottom surface of the top spacer (as shown in Figure 4.5b), ensuring direct contact with the top surface of the sample. The positioning of the sensors can be seen in Figure 4.5b. Furthermore, as illustrated in Figure 4.5c, the direction of the notches induces the propagation of cracks between pairs of sensors. Thus, these four sensors function collectively to identify crack propagation, although they do not specify the precise location in the axial orientation of the sample. It is important to point out that the same sensor, filters, waveforms, and AE timing parameters (Hit definition time (HDT), Hit lockout time (HLT) and Peak definition time (PDT)) were deployed for all experiments. The collected data comprises the number of events changing over time, the location of each event, and the hit rate. Acoustic emission data was obtained as the internal pressure increases, showing the changing event counts over time. It is noteworthy to mention that the hit rate was calculated based on the number of times any channel is activated by a signal, while an event necessitates the activation of at least three channels simultaneously

to receive hits. The AE monitoring results were evaluated together with the pressure records to determine whether rock breakage occurred prior to the peak pressure.

(a)
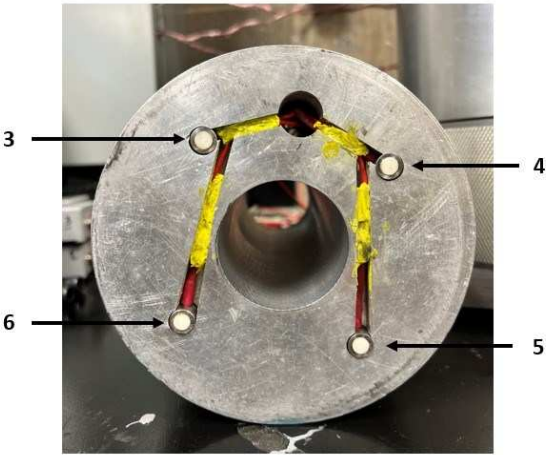
(b)

(c)

Figure 4.5: a) Acoustic emission monitoring system b) Sensors placed on the bottom of top spacer

c) Sensor pattern (after Zhang, 2019)

5 Results of Experiments

5.1 Burst Experiments with *W* = 12

5.1.1 Pressure Results

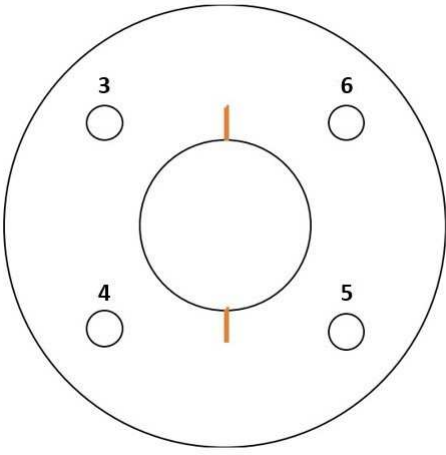In the first series of experiments, the geometry configuration was fixed with a 152.4 mm outer diameter and a 12.7 mm inner hole diameter, which means $w = 12$ (see Table 4.1). Thus, all parameters remain constant with the exception of pressure ratio, p^*. Three different pressure ratios have been applied in these tests, namely $p^* = 0$, $p^* = 1/8$ and $p^* = 1/6$. Also, all of these tests were carried out with the AE monitoring. To begin with, the inner pressure was increased at a constant rate of 6.2 MPa/min, starting from 2.5 MPa, while simultaneously the outer (confining) pressure was increased at 1.03 MPa/min (1/6 of the rate of the inner pressure) from 0.42 MPa, or 0.78 MPa/min (1/8 of the rate of the inner pressure) from 0.31 MPa.

Figure 5.1a highlights the first unconfined test ($p^* = 0$, test 1), where the inner pressure reaches 21.42 MPa, and the sample ruptures. This peak pressure is chosen as the critical inner pressure to estimate the fracture toughness via Equation (3.2). In other experiments with $p^* = 1/8$ (test 2) and $p^* = 1/6$ (test 3), the inner pressure ramps up to 68.95 MPa (shown in Figure 5.1), then a sudden decrease occurs in inner pressure. This happens as the pump reached its maximum capacity in these two experiments. Despite the relatively high 68.95 MPa inner pressure, the samples did not burst. For this reason, peak pressure cannot be chosen to estimate K_{IC}. Furthermore, the outer pressure remained stable at 4.80 MPa around 300 and 350 seconds for test 2 and test 3 according to the data acquisition system, whereas the pressure reading on the pump was correct during the test. Therefore, outer pressure values are corrected for both tests in Figure 5.1b and Figure 5.1c. In a word, the critical inner pressure for the first test has been chosen, corresponding to the pressure drop taken as evidence of the sample's rupture. However, the critical inner pressure for test 2 and test 3 is expected to be more than 68.95 MPa as the samples did not rupture and the experiments had to stop due to the pump failure. Normally, it is expected to have higher critical inner pressure with $p^* = 1/6$ than with $p^* = 1/8$ because the burst pressure increases with increasing confining pressure. The resulting estimate of K_{IC} will be presented in the next chapter.

(a)

(b)

(c)
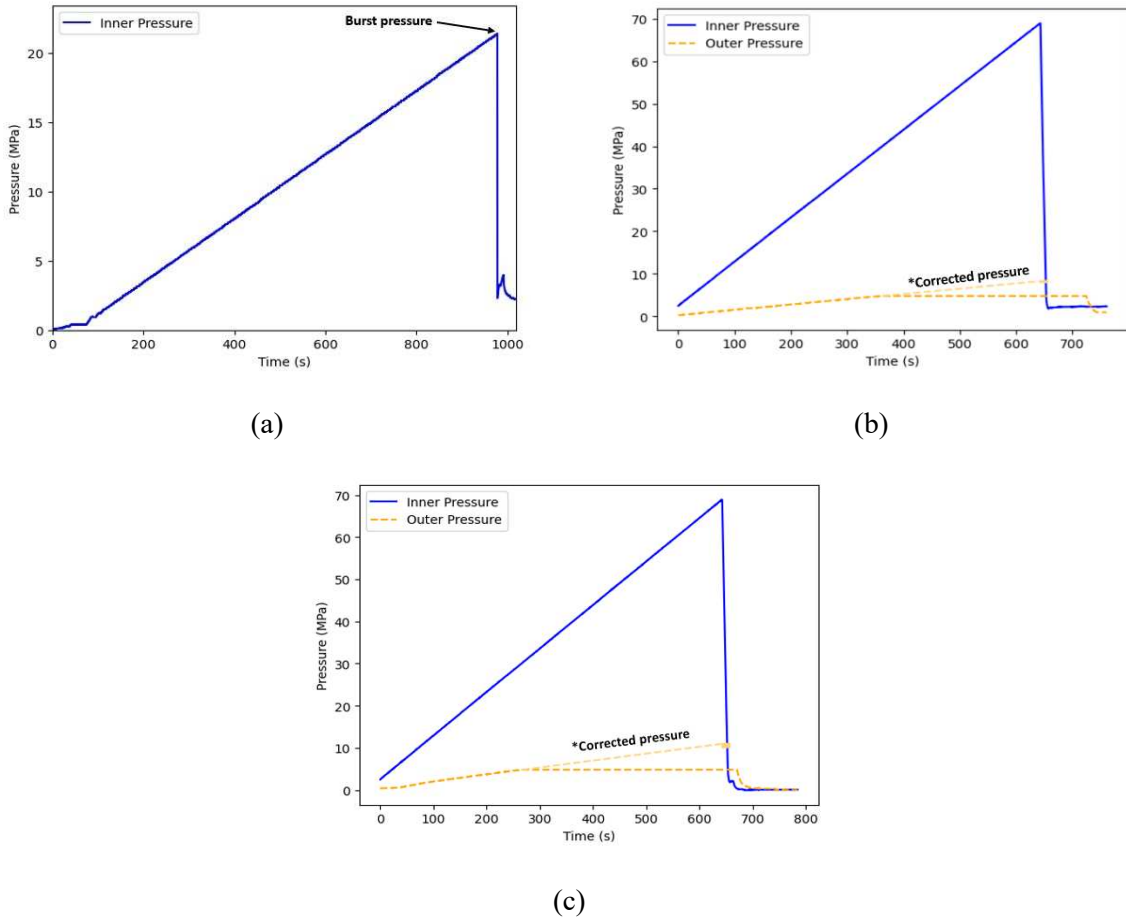
Figure 5.1: Pressure results for burst experiments with $w = 12$, (a) test 1 (unconfined), (b) test 2 ($p^* = 1/8$), (c) test 3 ($p^* = 1/6$)

5.1.2 AE Results

The SIF simulations predicted that there will be unstable growth for $w = 12$ with $p^* = 0$ and stable growth for $w = 12$ with $p^* > 0$. Therefore, tests with $p^* = 1/8$ and 1/6 are presented here in particular, which were predicted to have a period of stable growth before the rupture of the sample. Acoustic Emission (AE) monitoring results indicating significant generation of acoustic energy before the rupture of the sample will be taken as evidence of stable growth well before the peak pressure. Three sets of AE records for $w = 12$ are compared in this section: one from an unconfined test with unstable growth (Figure 5.2a), and two from confined tests with $p^* = 1/8$ and $p^* = 1/6$ that exhibited predicted stable growth (Figure 5.2b and Figure 5.2c). It is noteworthy to mention again that the samples did not rupture as the inner pressure pump maximum capacity was achieved before the rupture of samples for tests 2 and 3. However, the comparison of these series of AE records revealed a distinct difference, providing evidence of stable crack growth in the confined tests with $p^* = 1/8$ and $p^* = 1/6$. It is clear that the number of events grows in a different way for these two different crack growth types. For the unconfined test, predicted to have only unstable growth, the number of events kept almost unchanged before the

rupture of the sample. Then it suddenly increased, corresponding to the rupture of the sample determined by the pressure drop point shown in Figure 5.2a. However, for the confined test with $p* = 1/8$, with predicted stable growth, the number of events steadily increased from 0 to above 200 over a period of about 600 seconds of loading (Figure 5.2b). Then it suddenly grew from 250 to upwards, corresponding to the pump maximum achievable inner pressure capacity shown by the pressure drop point in Figure 5.2b. For the test with $p* = 1/6$, also with predicted stable growth, the AE monitoring records during this test showed steady growth of the event number again before the pressure peak. The number of events gradually increased from 0 to 18 over a period of 500 seconds of loading (Figure 5.2c). The number of recorded events with test 3 is less than that of with test 2, as test 2, with lower confining pressure, is close to the burst pressure at the time of maximum achievable pressure. The AE records demonstrate that AE events occur well before the peak pressure and increase over a long time period with variable acceleration for the tests expected to have stable growth (test 2 and test 3), whereas the number of events surges in relatively short time period at around peak pressure, corresponding to the rupture of the sample for unstable growth (test 1). In summary, a clear distinction is observed between stable and unstable growth, yet visual confirmation of micro cracks with microscopic investigation is necessary to validate the existence of stable crack growth.

(a)

(b)

(c)
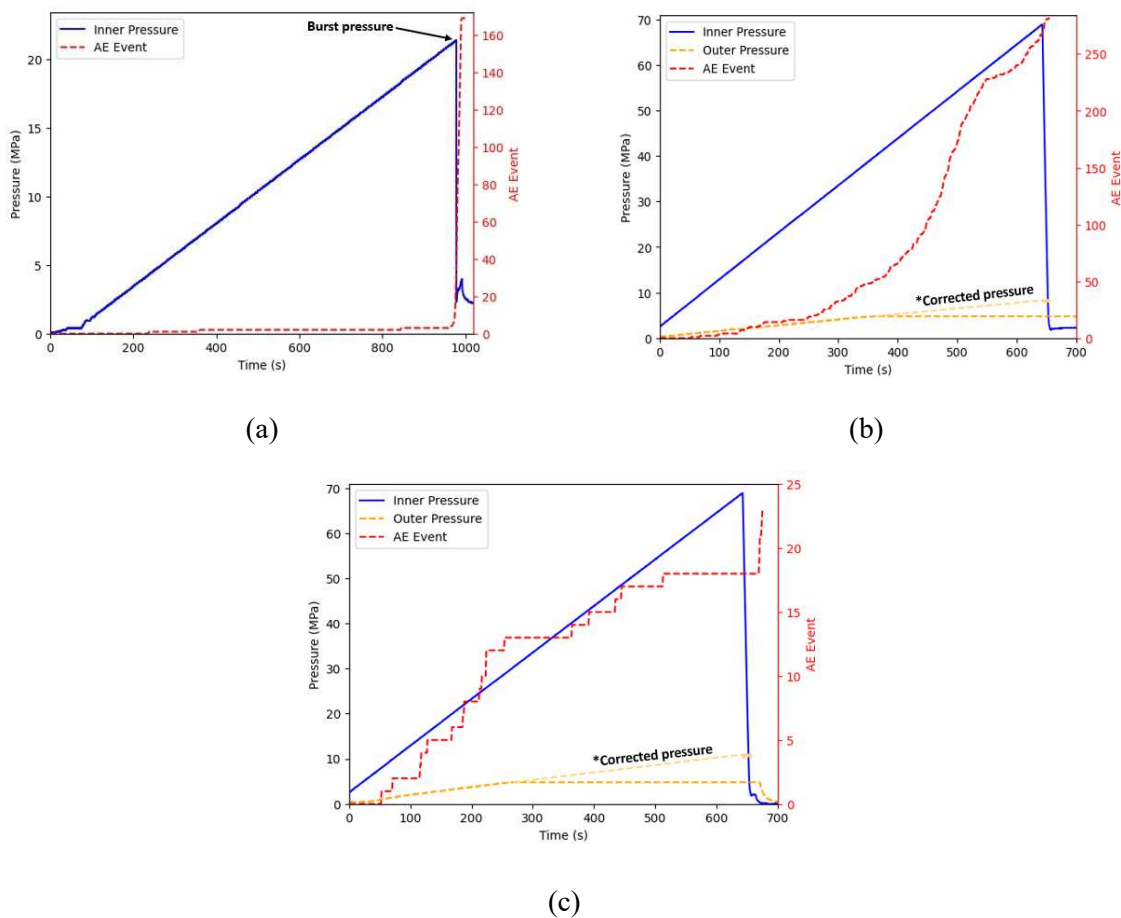
Figure 5.2: AE monitoring records corresponding to $w = 12$ tests, (a) test 1 (unconfined), (b) test 2 ($p* = 1/8$), (c) test 3 ($p* = 1/6$)
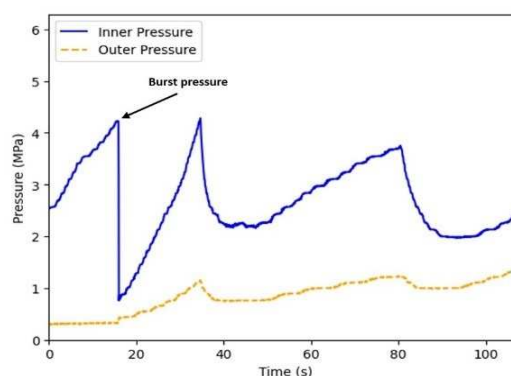
5.2 Burst Experiments with *W* = 3

5.2.1 Pressure Results

In contrast to the tests performed with $w = 12$, the burst tests involving $w = 3$ were anticipated to exhibit solely unstable crack propagation. These sets of burst experiments were performed with varying pressure ratios, while keeping all other parameters constant, as outlined in Table 4.1. Thus, applying the same characteristics of all previous tests, the initial internal pressure was 2.48 MPa, with a fixed rate of pressure increase at 6.2 MPa/min. The pressure ratio $p*$ (considered as 0, 1/8, and 1/6) stood out as the only variable in this series of experiments, while the dimensions w and the initial crack length of each sample remained fixed. Figure 5.3 displays the pressure records obtained from all experiments for $w = 3$.

The unconfined test ($p* = 0$, test 4) result with a sample having a 12.7 mm inner hole diameter is shown in Figure 5.3a. The inner pressure increased up to 3.67 MPa, and then the sample ruptured. This test resulted in a higher peak pressure value than expected because the sample did not fail along the initial notch direction for the other half of the sample (Figure 5.4). However, this peak pressure was selected to be the critical pressure to estimate fracture toughness. Then, a typical confined test with $p* = 1/8$ (test 5) was performed starting from 0.31 MPa, where the confining pressure was applied with an increase of 0.78 MPa/min (1/8 of the rate of the inner pressure). The inner pressure increased to 4.22 MPa (Figure 5.3b), after which the rupture of sample occured. Finally, two confined tests with $p* = 1/6$ (tests 6 and 7) were carried out with an initial confining pressure of 0.42 MPa, where the confining pressure was increased 1.03 MPa per minute (1/6 of the rate of the inner pressure). The peak pressure values of 5.79 MPa and 7.90 MPa were measured (Figure 5.3c and Figure 5.3d), respectively, which were used to estimate K_{IC}. It is sometimes the case that the inner pressure ramps up even after the first sudden pressure drop, which leads to two or more peaks of inner pressure over a certain period. In this situation, it is questionable which peak pressure should be chosen to estimate the fracture toughness of the notch. Our approach is to choose the first peak pressure corresponding to initial growth to prevent any overestimation of the K_{IC} value.

(a)

(b)

(c)   (d)
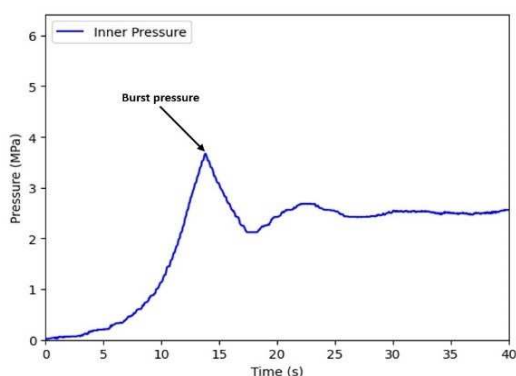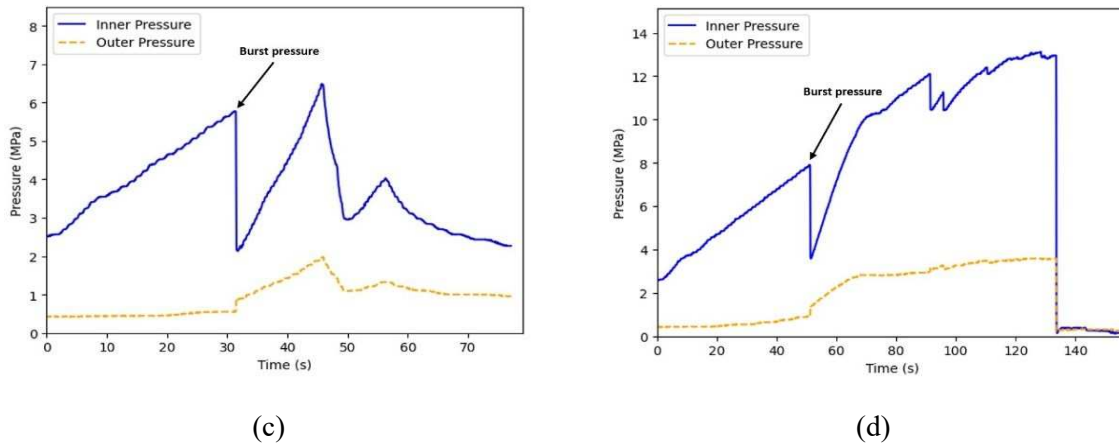
Figure 5.3: Pressure results for burst experiments with $w = 3$, (a) test 4 (unconfined),
(b) test 5 ($p^* = 1/8$), (c) test 6 ($p^* = 1/6$), (c) test 7 ($p^* = 1/6$)

Figure 5.4: Unexpected crack growth for the other half of the sample in unconfined test (test 1)

5.2.2 AE Results

The AE records obtained from burst experiments with $w = 12$ revealed notable distinctions between unstable growth and stable growth (recall Figure 5.2). However, SIF computations predicted only unstable growth for experiments with $w = 3$ configurations having $p^* = 0$, 1/8 and 1/6. Therefore, it is valuable to analyze the behavior of unstable growth in these AE records to compare to those previous experiments displaying potential stable growth.

For this reason, AE monitoring has been applied to the tests with $p^* = 1/8$ and $p^* = 1/6$ for $w = 3$. The peak burst pressures were chosen as 4.22 MPa and 5.79 MPa. For these tests a total number of 406 and 306 AE events were recorded, respectively. The AE records demonstrate similarities to the previous tests, showcasing unsteady growth only when $w = 12$ and $p^* = 0$. Compared to $w = 12$ and $p^* = 0$ few AE events were recorded for both tests (test 5 and test 6) at the beginning, but, likewise, the number of events surged massively in the last 10 seconds before the rupture of sample. The AE records for $p^* = 1/8$ case (test 5) showed that the number of events was around 20 until a sudden drop in inner pressure was observed. Then, the number of events dramatically increased to nearly 300 (Figure 5.5a). Similarly,

the AE records for $p^* = 1/6$ case (test 6) illustrated that the number of AE events increased remarkably from nearly 25 to above 200 in just ten seconds at the time of rupture. AE monitoring result for $p^* = 1/6$ case (test 6) is given in Figure 5.5b. This spike in the number of events for both tests is a significant indicator of unstable growth at the time of rupture. This result here highlights the characteristics of the test with unstable growth from AE using a different geometry configuration. Nonetheless, the cause of the limited number of events that occurred at the early stage remains ambiguous, and it cannot be excluded that they could be associated with unforeseen stable crack growth.


(a)   (b)
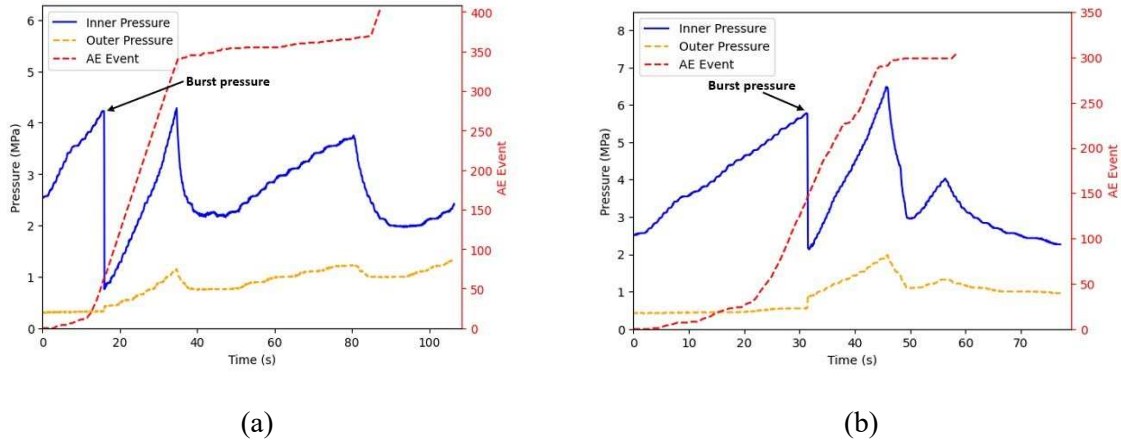
Figure 5.5: AE monitoring records corresponding to $w = 3$ tests, a) test 5 ($p^* = 1/8$), b) test 6 ($p^* = 1/6$)

5.3 Fixed Confinement Tests

The outer and inner pressures of the original burst experiment in Abou-Sayed (1978), increase proportionally, with a ratio of p^*. The initial inner pressure and the initial notch length were fixed in the previous tests. The main design purpose of the previous tests was to analyze the dependence on the pressure ratio p^* and the specimen configuration w. In this section, a series of tests with fixed confinement have been carried out to further evaluate the possible dependence of the behavior on confining pressure from another perspective. The results of SIF simulations were given in the Section 3.4.2 for the fixed confinement tests. Zhang (2019) have applied three levels of fixed outer pressure (1 MPa, 3 MPa and 4.8 MPa) on $w = 3$ geometry. In this study, the samples with $w = 12$ geometry have been exposed to the same outer pressure values to see the effect on different configuration. Also, AE monitoring was used for two tests to get clues about crack growth, where stable crack growth is expected according to results of SIF simulations. Eventually, three different outer pressure values (0.5 MPa, 3.5 MPa, and 6.5 MPa) have been applied on $w = 3$ geometry to expand the range of results on the samples with this geometrical configuration.

5.3.1 Results with *W* =12

As it is mentioned in the introduction three levels of outer pressure have been applied for tests with the *w* = 12 geometrical configurations, respectively 1 MPa, 3 MPa, and 4.8 MPa. The pictures of samples after the rupture are illustrated together with the pressure monitoring results in Figure 5.6. The peak pressures were measured as critical inner pressure values to estimate the K_{IC}, are 20.31 MPa, 40,45 MPa, and 53.87 MPa, respectively.
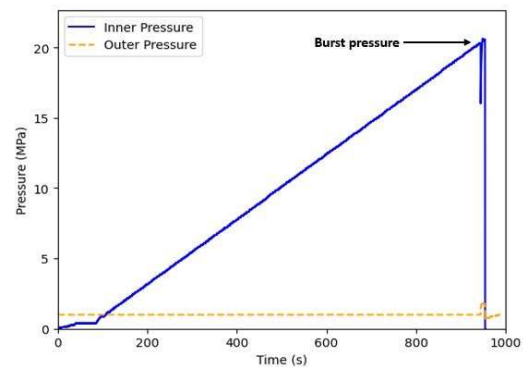
(a)
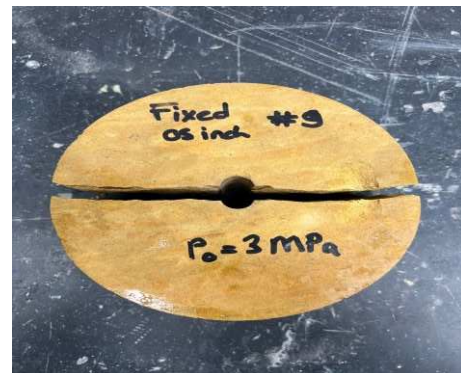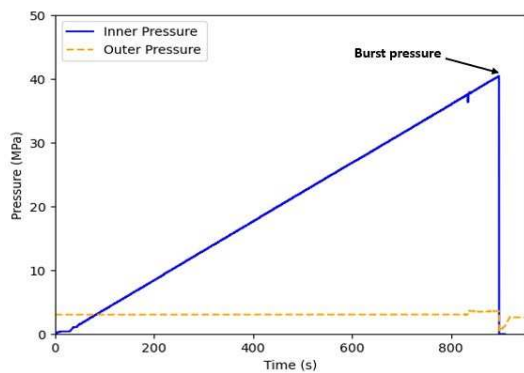
(b)
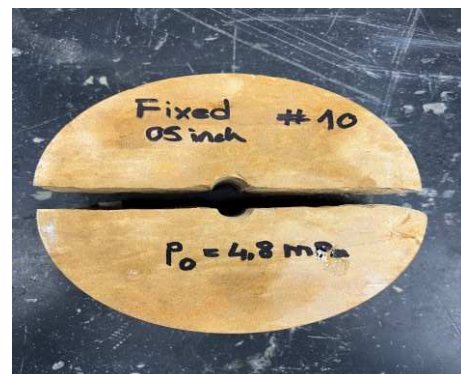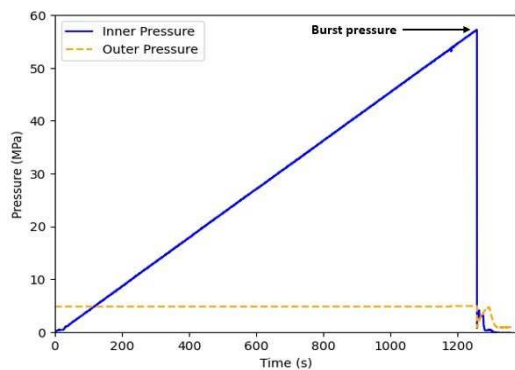
(c)

Figure 5.6: Tests with fixed confinement for *w* = 12 geometry as, (a) 1 MPa (F-1), b) 3 MPa (F-2), c) 4.8 MPa (F-3)

5.3.2 AE Results with *W* = 12

According to SIF computation results, a period of stable growth before the rupture of the sample was expected with $w = 12$ geometry under fixed confinement pressure. AE monitoring has been applied to those two tests (test F-2 and test F-3) having 3 MPa and 4.8 MPa constant outer pressure (Figure 5.7). During test number F-2, AE events were initially detected at around 600s into the experiment, for an inner pressure of approximately 25 MPa. Then, the number of events had a steep increase and reached over 600 at around 800s. Lastly, there was a slowdown in the rate of increase in number of events, as there was a slight decrease in inner pressure at around 90% of the peak pressure, but then the number of events has shown dramatic increase at the point of rupture, corresponding to peak pressure of 40.45 MPa. In experiment number F-3, more AE events were recorded in total, as the experiment took longer. However, the change in AE events over time was similar to the test number F-2. The number of AE events started to increase steadily at around 700s, and it accelerated as the pressure approached to the peak pressure at around 1100s. Also, there was a slight decrease in inner pressure just before the rupture of sample, where the increase rate of AE events slowed down. But then, the number of AE events increased from 1500 to nearly 1600 quite fast, after the rupture of sample at a peak pressure of 53.87 MPa.

(a)   (b)
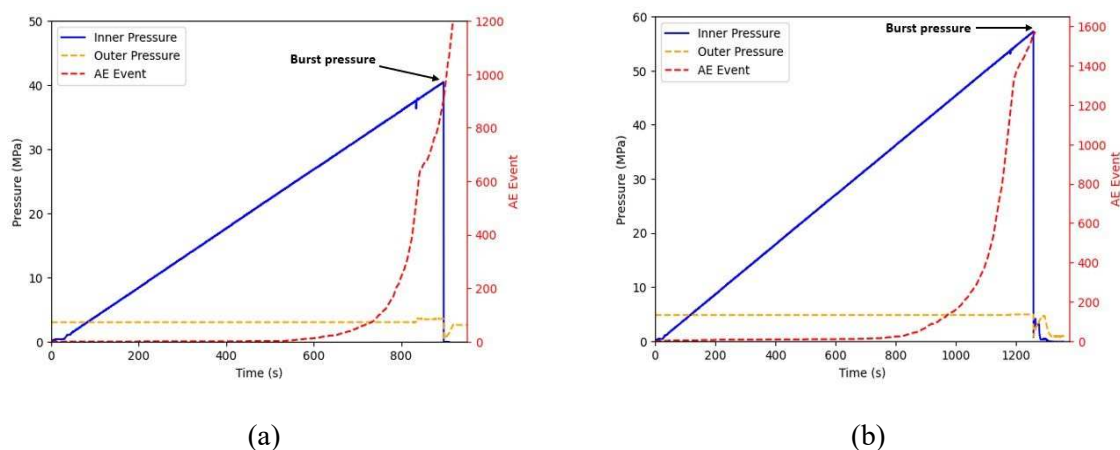
Figure 5.7: AE monitoring records for fixed confinement tests with $w = 12$,
a) 3 MPa (F-2), b) 4.8 MPa (F-3)

5.3.3 Results with *W* = 3

Confining pressure having three different values (0.5 MPa, 3.5 MPa, and 6.5 MPa) was applied for tests with the $w = 3$ geometry to enhance the range of outcomes in Zhang (2019) concerning samples featuring this specific geometrical arrangement. For all these experiments, inner pressure shows a steady increase until the point of rupture. The ruptured samples and the pressure monitoring results are shown in Figure 5.8. The peak pressures were measured as critical inner pressure values to estimate the K_{IC}, are 5.66 MPa, 12.28 MPa, and 21.25 MPa, respectively.
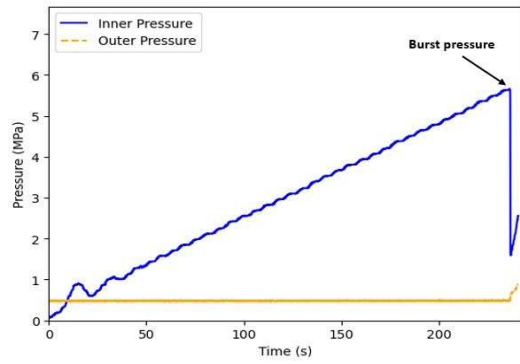
(a)
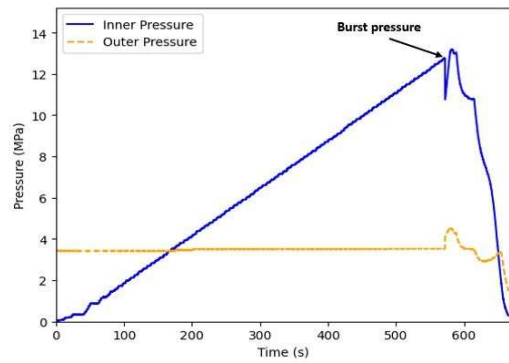
(b)
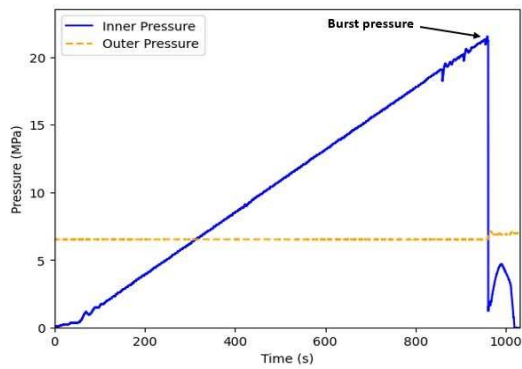
(c)

Figure 5.8: Tests with fixed confinement for *w* = 3 as, (a) 0.5 MPa (F-4), b) 3.5 MPa (F-5), c) 6.5 MPa (F-6)

6 Fracture Toughness (K_{IC}) Estimation

6.1 K_{IC} Calculation

The facture toughness of the burst experiment was determined using the critical pressure at the point of rupture (burst pressure), geometry, and computed SIF results, as described in Section 3.2. The fracture toughness was estimated for the experiments with $w = 3$ and $w = 12$ configurations having proportional pressure increase and fixed confinement pressure tests. The critical inner pressure point was identified for each test, as described in Section 5. In this chapter, K_{IC} was estimated for each case using Equation (3.2), with the results shown in Table 6.1. Moreover, for the tests with fixed confinement, K_{IC} results are shown in Table 6.2. K_{IC} varies significantly from 0.51 MPa$\sqrt{m}$ to 2.22 MPa$\sqrt{m}$. The fracture toughness estimations with proportional pressurized tests are generally lower than those with a fixed confinement pressure. For the $w = 3$ tests with $p^* = 1/8$ (test 2) and $p^* = 1/6$ (test 3), respectively, the K_{IC} values cannot be estimated properly, as the pump has reached its maximum capacity of 68.95 MPa and the experiment stopped before the rupture of samples. However, K_{IC} values were calculated based on maximum achieved pressure value of 68.95 MPa for both cases to ensure integrity of calculations, which normally does not reflect the reality. Therefore, these results were marked with ''*'' in Table 6.1. In addition to the proportional pressure tests, six experiments were run with fixed confinement pressure to investigate the dependence of K_{IC} on confinement. The K_{IC} values show a steady increase, as confining pressure increases in fixed confinement pressure experiments. In these two different experiment designs, K_{IC} estimations of the $w = 12$ geometry have almost double the K_{IC} results with as those $w = 3$ geometry.

Table 6.1: Summary of K_{IC} estimations for $w = 3$ and $w = 12$ experiments (the "Stability" column is a prediction based on the global stability criterion (see Section 3.3); "AE" means test with AE monitoring)

Test Name	Stability	Hole Diameter (mm)	w (b/a)	p^* (P_o/P_i)	p^*w	P_i (MPa)	K_{IC} (MPa$\sqrt{m}$)
1, AE	unstable	12.7	12	0	0	21.42	1.28
2, AE	stable	12.7	12	1/8	1.5	*68.95	*2.22
3, AE	stable	12.7	12	1/6	2	*68.95	*1.59
4	unstable	50.8	3	0	0	3.67	0.61
5, AE	unstable	50.8	3	1/8	0.375	4.22	0.51
6, AE	unstable	50.8	3	1/6	0.5	5.79	0.62
7	unstable	50.8	3	1/6	0.5	7.90	0.85

Table 6.2: Summary of K_{IC} estimations for fixed confinement experiments (note the "Stability" column is a prediction based on the global stability criterion (see Section 3.3); "AE" means test with AE monitoring)

Test Name	Stability	Fixed (P_o)	w (b/a)	p^* (P_o/P_i)	p^*w	P_i (MPa)	K_{IC} (MPa$\sqrt{m}$)
F-1	Stable /Unstable	1	12	0.05	0.60	20.31	1.00
F-2, AE	Stable	3	12	0.08	0.96	40.45	1.70
F-3, AE	Stable	4.8	12	0.09	1.08	53.87	2.21
F-4	Unstable	0.5	3	0.09	0.27	5.66	0.77
F-5	Unstable	3.5	3	0.27	0.81	12.28	0.90
F-6	Unstable	6.5	3	0.31	0.93	21.25	1.30

6.2 Dependence of Fracture Toughness on Configuration

This section highlights the analysis of the configurational dependence of K_{IC}. Given that the experiments involve two distinct independent variables, namely the pressure ratio p^* and the radius ratio w, the decision was made to designate the x-axis as p^* and divide it into groups based on different w tests.

One aspect under consideration is the analysis of the K_{IC} estimations within each group sharing identical hole size. For the burst experiments conducted with $w = 3$, characterized by unstable crack growth, it can be said that there is a direct proportional relationship between K_{IC} and p^*. The only point to consider is that the unconfined test ($p^* = 0$) resulted with a little bit higher K_{IC}, as the sample did not break through the initial notch from the other half (recall Figure 5.4). Conversely, in the $w = 12$ group, this correlation is not evident, possibly due to the stable crack growth pattern.

Another aspect under consideration is to assess the dependence of the tests on p^* and w, when examining the results between each set of tests with the same p^* but different w. Detailed analysis reveals that tests conducted with smaller hole sizes (larger w) resulted in higher values for the calculated K_{IC}. Notably, even in the unconfined test ($p^* = 0$), the K_{IC} value obtained from the 12.7 mm hole diameter configuration ($w = 12$) was approximately twice as large as the K_{IC} value obtained from the 50.8 mm hole diameter configuration ($w = 3$). Although K_{IC} value cannot be estimated appropriately for proportional pressure tests ($p^* = 1/8$ and $p^* = 1/6$) with $w = 12$ configuration in this study, the results were also more than twice the K_{IC} from $w = 3$ configuration. K_{IC} estimations cannot be done accurately since the pump capacity did not allow us to measure the burst pressure of $w = 12$ tests with $p^* = 1/8$ and $p^* = 1/6$. However, K_{IC} of the $w = 3$ tests with $p^* = 1/6$ was greater than that of the test with $p^* = 1/8$ in this study, which confirms previous studies. Similar to this study, Yoshioka et al. (2023) also showed

that the K_{IC} of the test with $p* = 1/6$ is larger than that of the test with $p* =1/8$ with $w = 3$ configuration, which is contrary to results from $w = 12$ tests. The influence of stress ratio on K_{IC} became more evident in the burst experiments conducted with $w = 3$. For the $w = 12$ tests, the samples did not break in test 2 and test 3, although maximum pump capacity was reached. Due to this situation, higher values are expected, and this is indicated with a (>) sign in Figure 6.1. In general, the configurational dependence of the results for proportional burst experiments is presented in Figure 6.1.
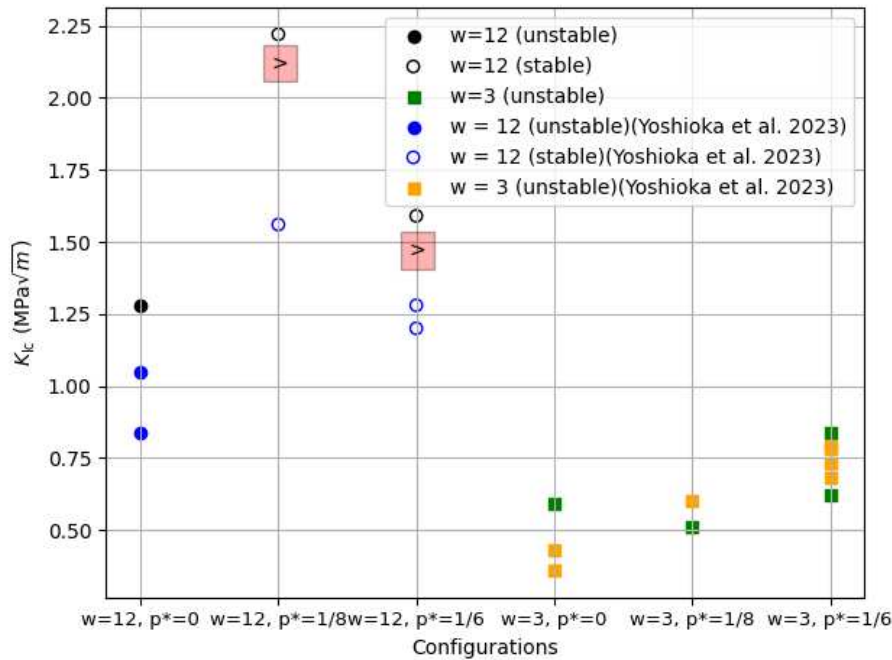

Figure 6.1: Configurational dependence of the K_{IC} results for proportional pressure burst experiments
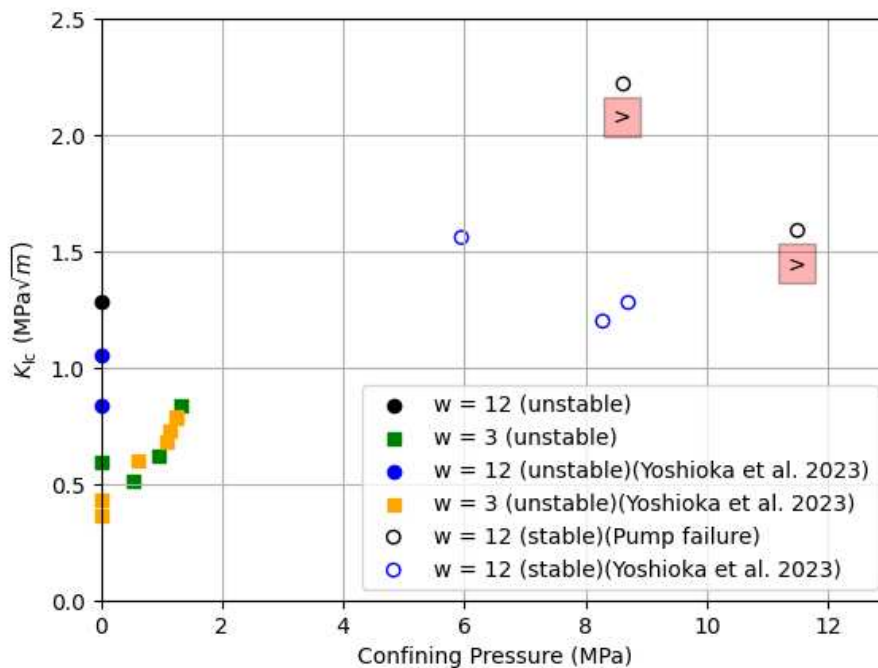
6.3 Dependence of Fracture Toughness on Confinement

6.3.1 Evaluation of *W* = 3 and *W* = 12 Tests

Previous burst experiments have shown that K_{IC} is influenced by the confining pressure (Figure 1.1). This section examines the possible dependence of K_{IC} on confinement in $w = 3$ and $w = 12$ burst experiments with possible stable and unstable growth. The comparison of the results between this study and Yoshioka et al. (2023) with the $w = 3$ and $w = 12$ configurations is given in Figure 6.2 as a function of confining pressure.

The $w = 12$ configuration tests with $p* = 1/8$ and $p* = 1/6$ were predicted to have stable crack growth, whereas none of the $w = 3$ tests were expected to be stable in the global stability criterion. As it was mentioned in the previous section that higher K_{IC} values are expected in reality for test 2 and test 3. However, even with the accurate case, the distribution of the K_{IC} results as a function of the confining pressure on the graph would be more or less the same, as both will have a certain increase. With all other variables the same except the geometrical configuration, it is observed that the lower-bound values of

K_{IC} calculated from $w = 12$ tests with $p^* = 1/8$ and $p^* = 1/6$ are larger than those for $w = 3$. The results from these tests show an unanticipated negative correlation with increasing confining pressure (Figure 6.2). This negative correlation was also found in Yoshioka et al. (2023) for the stable crack growth of $w = 12$ tests with $p^* = 1/8$ and $p^* = 1/6$. When we consider all these findings for stable growth in Section 6, it is challenging to interpret the relationship between fracture toughness and confinement in stable experiments.

For the $w = 12$ tests, only the unconfined pressure test (test 1) was predicted to have unstable crack growth. This test resulted in a larger K_{IC} than that of the unconfined pressure test $w = 3$. Unlike for $w = 12$, all $w = 3$ tests were predicted to be unstable in the global stability criterion according to SIF simulation results. The AE records also indicate that the $w = 3$ series of tests exhibits solely unstable crack growth as was observed in Yoshioka et al. (2023). Figure 6.2 illustrates a clear linear positive correlation between K_{IC} and the confining stress for experiments with unstable crack growth, which is in agreement with the results reported in the literature already mentioned in Section 4.2.1. The K_{IC} of test 4 was higher than expected, as the sample failed in an unexpected way (recall Figure 5.4).

Figure 6.2: Fracture toughness (K_{IC}) as a function of the confining pressure P_o for $w = 3$ and $w = 12$

6.3.2 Evaluation of Fixed Confinement Tests

In this section, we focus on investigating the dependence of K_{IC} on confinement and analyzing the results from fixed confinement tests. It should be noted that three distinct values of confining pressure are applied in the tests for two different configurations ($w = 3$ and $w = 12$). Since 1 MPa, 3 MPa, and 4.8 MPa confining pressures have already been applied on $w = 3$ geometry in Zhang (2019), the confining pressures have been adjusted to 0.5 MPa, 3.5 MPa, and 6.5 MPa on the same geometry to expand the

range of applications in this study. But then, the same three values of fixed confining pressure in Zhang (2019) were applied on the $w = 12$ configuration. The K_{IC} results vary between 0.77 MPa$\sqrt{m}$ to 2.21 MPa$\sqrt{m}$, having greater values for $w = 12$ configuration than $w = 3$ configuration (Figure 6.3). Furthermore, all tests with $w = 12$ geometry were predicted to have stable crack growth, whereas all $w = 3$ tests were predicted to be unstable in the global stability criterion according to SIF simulation results. It is also observed that the K_{IC} increases for both configurations with increasing confining pressure regardless of stable or unstable crack growth. When we compare the K_{IC} results with Zhang's study, it is seen that relatively higher K_{IC} values have been estimated in this study. This may be due to the differences in the characteristics of the samples taken. One important point is to consider that Zhang (2019) shows stable crack growth with 4.8 MPa for the w = 3, whereas the SIF simulation predicted unstable crack growth with 6.5 MPa confining pressure, as also observed with the experiment. This change in crack growth type from unstable to stable and back to unstable with increasing confining pressure is difficult to interpret without considerable additional experimentation.
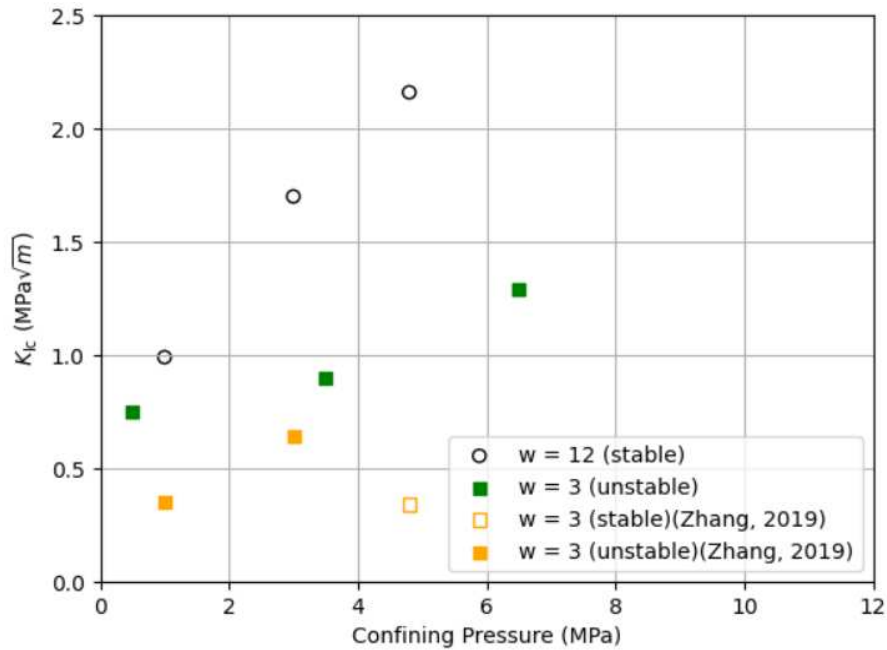
Figure 6.3: Fracture toughness (K_{IC}) as a function of the confining pressure with fixed confining pressure P_o for $w = 3$ and $w = 12$

7 Recommendations

The suggestions for upcoming implementation and research using burst experiments are outlined as follows:

1. For configurations with stable crack growth, there is a possibility to overestimate the fracture toughness. In order to ensure accurate estimation of K_{IC} and to avoid the possibility of spurious dependence of fracture toughness on confining stress, it is preferable to use unstable configurations. It is crucial to conduct additional research on the existence of stable crack growth. One possible investigation might be artificially stopping a burst experiment just before the point of rupture and then cutting the sample layer by layer for an investigation either by naked eye or under microscope. This method could offer more insights compared to the current procedure. The presence of observable evidence can enhance the ability to definitively ascertain the presence of stable crack growth. Another possibility might be the use of developed sensor distribution or a method, which enables researchers to detect reliable location of the events over the experiments.

2. It must also be noted that the specifications of AE monitoring system play a key role in receiving the number of hits and accordingly events. The range of specifications must be carefully arranged before the test, so that reliable monitoring results can be achieved. These specifications are still questionable and require additional experiments for critical assessment of accuracy and reliability.

3. From a practical standpoint, it is more advisable to employ a larger inner hole size when undertaking a burst experiment. This is due to the fact that utilizing a smaller hole size would result in higher overall pressures during the test. As a result, these higher overall pressures are associated with increased rates of test failure.

4. Before running the test, the sample can be covered with a thin, protective transparent sheet layer to prevent penetration of the confining pressure fluid into the sample and the effect of this oil on microcrack development in the case of leakage into the burst cell.

8 Conclusion

This study focuses on the identification of stable crack growth in the burst experiment, illustrating its implications, and suggesting modifications to address the challenges it presents. The key contributions of this research can be summarized as follows:

It was demonstrated that the SIF predictions were efficient in identifying configurations that lead to unstable and stable crack growth based on global stability criterion. If K_I^{B*} increases monotonically with ℓ increasing, there will be unstable crack growth. Otherwise, it is anticipated that there will be a presence of stable crack growth if K_I^{B*} decreases monotonically with ℓ increasing, which can lead to overestimation of K_{IC}.

The characteristics of AE monitoring records provide valuable insights in terms of investigating crack growth. Generally, the records obtained from tests predicting stable growth exhibit dissimilar characteristics compared to those predicting only unstable growth. Over time, the stable growth tests demonstrate a gradual and steady increase in the number of events, whereas the number of events increases remarkably either at the point of burst or short before the point of burst with unstable growth tests. The acoustic emission monitoring method demonstrated that stable crack propagation normally occurs well before the final failure, which might lead to an overestimation of fracture toughness when it is calculated using the ultimate peak pressure result according to the original test procedure.

The global criterion of stability predictions has been compared and verified with the recordings of AE monitoring system. The SIF predictions generally show the correct type of stable and unstable crack growth. It is noteworthy to mention that specifications of AE monitoring system have a vital importance in recording the number of hits and events. In this study, AE records generally met and verified the predicted crack growth type in the SIF simulation results.

The relationship between K_{IC} and confinement has been examined through proportional pressurized and fixed confinement experiments. When considering only unstable growth a linear positive correlation is observed between K_{IC} and confining pressure for both experiments. However, a downward trend is observed between K_{IC} and confinement pressure considering the results of proportional pressurized experiment with stable crack growth, whereas K_{IC} results increase with increasing confining pressure in fixed confinement tests.

In summary, the AE records indicate a stable growth pattern prior to specimen rupture, potentially leading to inaccurate K_{IC} estimation. Furthermore, the dependence of K_{IC} results on confinement for stable tests is not as clear as in unstable test configurations. In cases of unstable crack growth, there is always a direct positive correlation between K_{IC} and confining pressure for both proportional pressurized and fixed confinement tests. The global stability criterion can be utilized in future research endeavors to develop burst experiments, followed by employing sophisticated analyses of AE outcomes. The

implementation of further tests would contribute to a clearer comprehension of the nature of stable crack growth, as well as insights into the underlying mechanical factors and predictive capabilities concerning the fracture toughness estimations under confining pressure

Acknowledgements

References

URL-1: Stress intensity factor - Wikipedia. Retrieved March 24, 2024, from
https://en.wikipedia.org/wiki/Stress_intensity_factor

URL-2: OpenGeoSys. Retrieved March 24, 2024, from https://www.opengeosys.org/

URL-3: Gmsh: a three-dimensional finite element mesh generator with built-in pre- and post-processing facilities. Retrieved March 24, 2024, from https://gmsh.info/

Abou-Sayed. (1978). An experimental technique for measuring the fracture toughness of rocks under downhole stress conditions.

Clifton, R. J., Simonson, E. R., Jones, A. H., & Green, S. J. (1976). Determination of the critical-stress-intensity factor from internally pressurized thick-walled vessels.

Destuynder, P., Djaoua, P. E. M., Chesnay, L., & Nedelec, J. C. (1981). Sur une Interprétation Mathématique de l'Intégrale de Rice en Théorie de la Rupture Fragile. Mathematical Methods in the Applied Sciences, 3(1), 70–87. https://doi.org/10.1002/mma.1670030106

Dubois, F., Chazal, C., & Petit, C. (1999). A Finite Element Analysis of Creep-Crack Growth in Viscoelastic Media. In Mechanics of Time-Dependent Materials (Vol. 2).

Erdogan, F. (2000). Fracture mechanics. www.elsevier.com/locate/ijsolstr

Griffith, A. A. (1921). VI. The phenomena of rupture and flow in solids. Philosophical Transactions of the Royal Society of London. Series A, Containing Papers of a Mathematical or Physical Character, 221(582–593), 163–198. https://doi.org/10.1098/rsta.1921.0006

Griffith, A. A. (1924). Griffith's Theory of Rupture. In C. B. Biezeno & J. M. Burgers (Eds.), International Congress for Applied Mechanics (pp. 55–63). J. Waltman.

Huang, Y., Zolfaghari, N., & Bunger, A. P. (2022). Cohesive element simulations capture size and confining stress dependence of rock fracture toughness obtained from burst experiments. Journal of the Mechanics and Physics of Solids, 160. https://doi.org/10.1016/j.jmps.2022.104799

Irwin, G. R. (1957). Analysis of Stresses and Strains Near the End of a Crack Traversing a Plate. Journal of Applied Mechanics, 24(3), 361–364. https://doi.org/10.1115/1.4011547

Ko, T., & Kemeny, J. (2007). Effect of confining stress and loading rate on fracture toughness of rocks. In Rock Mechanics: Meeting Society's Challenges and Demands (pp. 625–629). Taylor & Francis. https://doi.org/10.1201/NOE0415444019-c76

Kuruppu, M. D., Obara, Y., Ayatollahi, M. R., Chong, K. P., & Funatsu, T. (2014). ISRM-Suggested Method for Determining the Mode I Static Fracture Toughness Using Semi-Circular Bend Specimen. Rock Mechanics and Rock Engineering, 47(1), 267–274. https://doi.org/10.1007/s00603-013-0422-7

Lu, G., Gordeliy, E., Prioul, R., Aidagulov, G., Uwaifo, E. C., Ou, Q., & Bunger, A. P. (2020). Time-Dependent Hydraulic Fracture Initiation. Journal of Geophysical Research: Solid Earth, 125(3). https://doi.org/10.1029/2019JB018797

References

Lu, Q., Lu, G., Prioul, R., Aidagulov, G., & Bunger, A. P. (2018). Impact of Fluid Acidity on the Time-Dependent Initiation of Hydraulic Fractures in Carbonate Rocks. Rock Mechanics and Rock Engineering, 51(12), 3895–3906. https://doi.org/10.1007/s00603-018-1544-8

M. Erwan Tanné. (2017). Variational phase-field models from brit- tle to ductile fracture: nucleation and propagation. [PhD Thesis]. Université Paris-Saclay, École Polytechnique.

Roegiers, J.-C., & Zhao, X. L. (1991). Rock fracture tests in simulated downhole conditions: proceedings of the 32nd U.S. Symposium, the University of Oklahoma, Norman, 10-12 July 1991. A.A. Balkema.

Schmidtt, R. A., & Huddler, C. W. (1977). Effect of Confining Pressure on Fracture Toughness of Indiana Limestone. In Int. J. Rock Mech. Min. Sci. & Geomech. Abstr (Vol. 14). Pergamon Press.

Suo, X.-Z., & Combescure, A. (1992). On the application of G(Θ) method and its comparison with De Lorenzi's approach. Nuclear Engineering and Design, 135(2), 207–224. https://doi.org/10.1016/0029-5493(92)90223-I

Thallak, S., Holder, J., & Gray, K. E. (1993). The Pressure Dependence of Apparent Hydrofracture Toughness. In Int. J. Rock Mech. Min. Sci. & Geomech. Abstr (Vol. 30, Issue 7).

Yoshioka, K., Zhang, Y., Lu, G., Bunger, A., Adachi, J., & Bourdin, B. (2023). Improving the Accuracy of Fracture Toughness Measurement in Burst Experiments. Rock Mechanics and Rock Engineering, 56(1), 427–436. https://doi.org/10.1007/s00603-022-03097-y

Zhang, Y. (2019). Title Page Stress Dependence of the Burst Experiment for Determining Fracture Toughness.